Universidade de Aveiro Departamento de Física
Ano 2014/2015

Alexandre Faia Carvalho

Síntese simultânea de diamante em grafeno para aplicações eletrónicas

Simultaneous synthesis of diamond on graphene for electronic applications

Universidade de Aveiro Departamento de Física
Ano 2014/2015

Alexandre Faia Carvalho

Síntese simultânea de diamante em grafeno para aplicações eletrónicas

Simultaneous synthesis of diamond on graphene for electronic applications

Dissertação apresentada à Universidade de Aveiro para cumprimento dos requisitos necessários à obtenção do grau de Mestre em Engenharia Física, realizada sob a orientação científica da Doutora Florinda Mendes da Costa, Professora Associada do Departamento de Física da Universidade de Aveiro e do Doutor João Pedro dos Santos Hall Agorreta de Alpuim, Professor Auxiliar do Departamento de Física da Universidade do Minho.

Trabalho desenvolvido no âmbito dos projeto PTDC/CTM-NAN/117284/2010 e UID/CTM/50011/2013 financiados por fundos nacionais pela FCT/MEC e cofinanciado pelo FEDER sob o acordo de parceria PT2020.

Dedico este trabalho aqueles que sempre tudo me deram e à chata que só me parou de fazer cócegas quando fiquei maior que ela.

o júri

presidente

Prof.ª Doutora Teresa Maria Fernandes Rodrigues Cabral Monteiro
Professora associada com agregação do Departamento de Física da Universidade de Aveiro

orientadora

Prof.ª Doutora Florinda Mendes da Costa
Professora associado do Departamento de Física da Universidade de Aveiro

arguente

Doutor Jérôme Gilles Ollivier Borme
Investigador do quadro do INL - International Iberian Nanotechnology Laboratory

agradecimentos

Desde já agradeço à Professora Doutora Florinda da Costa, ao Dr. António José Silva Fernandes e ao Professor Doutor João Pedro dos Santos Hall Agorreta de Alpuim pelo apoio e orientação dados ao longo do desenvolvimento deste trabalho.

Agradeço ainda ao INL - International Iberian Nanotechnology Laboratory a oportunidade de estágio nas suas instalações, bem como a todos os que me acompanharam e acolheram, desde o Júnior ao Jérôme, passando pelas senhoras do refeitório que teimavam em tratar-me por Doutor.

Ao I3N pelo financiamento e completa abertura dos seus laboratórios para a realização de todo o trabalho experimental.

Ao Tiago, ao Nuno e ao restante pessoal do laboratório, um muito obrigado por toda a ajuda e tempo partilhado à procura das pinças desaparecidas ao longo destes três anos.

Um agradecimento à Marta, e ao Manuel pela colaboração na caracterização por TEM e EFM, e ao senhor Ivo e Miguel pela paciência e disponibilidade demonstradas.

A toda a comunidade do Departamento de Física da Universidade de Aveiro, docentes e não docentes, e colegas, que contribuíram para que estes 5 anos passassem como se em casa, e cujo nome de todos não caberia nesta página.

Devo indicar ainda neste agradecimento aqueles muitos outros tão especiais, e que sabem a importância que têm para mim.

Por último um grande abraço às senhoras da cantina que me alimentaram nestes anos!

Aveiro é nosso!

palavras-chave Grafeno, Diamante nano-cristalino, Híbridos de carbono, GDH, MPCVD, GFET

resumo

Neste trabalho é descrito o estudo de estruturas híbridas de grafeno e diamante nano-cristalino (GDH) sintetizadas por deposição química em fase vapor por plasma de micro-ondas (MPCVD) em cobre. Foram investigadas técnicas de controlo da nucleação do diamante nano-cristalino, tendo sido encontrados dois processos com sucesso. Procedeu-se ainda à caracterização estrutural, morfológica e ótica das amostras por análise de SEM, TEM, AFM, EFM, medidas de transmitância UV-Vis e espetroscopia de Raman. A avaliação das propriedades de transporte destes materiais foi efetuada pela medição da curva de transferência de transístores de efeito de campo produzidos para o efeito, sendo os GDHs produzidos o material ativo do canal. Foram observadas baixas mobilidades devido à hidrogenação do grafeno. Em linha com resultados teóricos da literatura, foram encontradas evidências de abertura do hiato energético do grafeno, um potencial desenvolvimento para a aplicação em dispositivos de comutação lógica.

keywords Graphene, Nano-crystalline diamond, Carbon hybrids, GDH, MPCVD, GFET

abstract In this work, hybrid structures of graphene and nano-crystalline diamond (GDH) produced by microwave plasma chemical vapor deposition (MPCVD) in copper substrates are studied. The control of the diamond clusters nucleation was investigated, having two different approaches been identified as promising. Structural, morphological and optical characterization was carried out by SEM, TEM, AFM, EFM, UV-Vis transmittance, and Raman spectroscopy. The transport properties of this material were analyzed through the transfer curve of field-effect transistors with GDH channels. Low mobilities were found due to graphene hydrogenation. In line with theoretical studies, evidences were found of graphene band gap opening, a potential breakthrough for the development of logical switching devices.

Content

List of Figures

List of Tables

Introduction

Carbon has been one of the most relevant elements in the development of humanity, either by its presence in a diversity of compound materials or by the outstanding properties of its allotropes. The 3-dimensional graphite and diamond were the only known forms of crystalline carbon until the discovery of the 0D fullerenes [1] and the 1D carbon nanotubes [2]. The 2D carbon structure, graphene, theorized in 1947 [3] remained elusive and even thought to be unstable at room conditions until 2004, when A. K. Geim and K. S. Novoselov successfully insulated this allotrope by peeling a single layer from a graphite chunk with no more than scotch tape [4]. Graphene had finally come to the world, being its discovery awarded with the 2010 Nobel Prize in Physics [5].

The interest in this 2D material comes mainly from its intrinsic properties such as electrical and thermal conductivity associated with a high intrinsic hole and electron mobilities [4, 6], chemical stability [7], high Young modulus [8], optical transparency [9], and room temperature Quantum Hall Effect [10]. Moreover, the 2D nature of graphene further increases its interest as it permits the development of a new class of nanoscale devices [11] or even the production of supercapacitors and other devices where high area to volume ratios are required [12, 13].

In the last years a big development was made around the large production of graphene. Nowadays, graphene is produced by various techniques, each suitable for a range of applications. Graphene mechanically exfoliated from highly-oriented pyrolytic graphite (HOPG) is by far the best for electronic applications as its low defects density preserves the electronic properties of graphene [4, 6]. However, the low throughput of this technique and the small size of the graphene sheets obtained from it hinders its potential for scalability. Epitaxial high-quality graphene can also be obtained by SiC reduction [14], however the transfer of the graphene grown by this technique to a chosen substrate is difficult. Chemical Vapor Deposition (CVD) on metals, namely copper and nickel has proven to be the most viable choice for the large scale production of graphene sheets [15, 16]. Thermal Chemical Vapor Deposition (TCVD) graphene grown on copper is presently the most common technique for graphene in electronic applications, as the high quality films are easily transferred from the original substrate to a chosen new one and continuous roll-to-roll production of graphene is already a reality [17]. Graphene obtained by liquid exfoliation or wet chemical processes is the one with best throughput, however, due to its relatively poor electrical properties, it is only suitable for applications where graphene takes part on a compound material, or in biological applications where this highly defective forms of graphene are suitable for functionalization [18, 19].

My bachelor dissertation was carried with the goal to explore the Microwave Plasma Chemical Vapor Deposition (MPCVD) technique for the fast production of graphene on copper substrates. Graphene was synthesized all over the 10×10 mm^2 copper substrates. However,

not only graphene was identified on the samples: nano-crystalline diamond (NCD) clusters were found sprinkled all over the sample.

Hybrid carbon materials, where different carbon allotropes combine their distinct outstanding properties have been studied in the last years [13, 20–22]. Graphene and diamond hybrids (GDH) have shown to be good candidates for field emission applications [13, 23], electronic devices, as diamond substrates increase the current carrying capacity of graphene due to its superior heat-sing properties [24], and even theoretical models shown that in some configurations the interaction with diamond promotes the appearance of a band-gap in graphene [25]. This last prediction would be of the highest importance in the actual application of graphene as the active material for field effect transistors to be used in logical circuitry, as it would allow an off state where energy would not be consumed, and higher on/off ratios, something not possible with graphene only because of its null band gap [26]. However, besides all the research in GDH's no report has yet been made in their simultaneous synthesis.

In this work, different approaches to vary the diamond phase in MPCDV grown GDH's were studied. The synthesis, characterization, transfer and field effect transistors device fabrication processes are described, and their results discussed.

Graphene

Structure and Properties

Graphite, the sp^2 bulk form of carbon, is known for its structure comprising stacked sheets of honeycomb like lattice. An individual sheet is know as graphene. In fact the name graphene has been used for diverse number of layers, from single layer graphene (SLG), bi-layer graphene (BLG) to Multi-layer graphene (MLG). Graphene lattice is a 2D hexagonal lattice with a bi-atomic motive, forming its characteristic honeycomb 2D sp^2 structure (Figure 1) [27]. This structure was thought to be unstable due to the Mermin–Wagner theorem which states that no ordered structures can exist at non 0 K temperatures for dimensions below 3 [28]. However graphene is found to be stable. This stability arises from the observed long range intrinsic ripples found on graphene. Nevertheless it was also shown that the interaction with the substrate allows graphene to exist in a flat form.

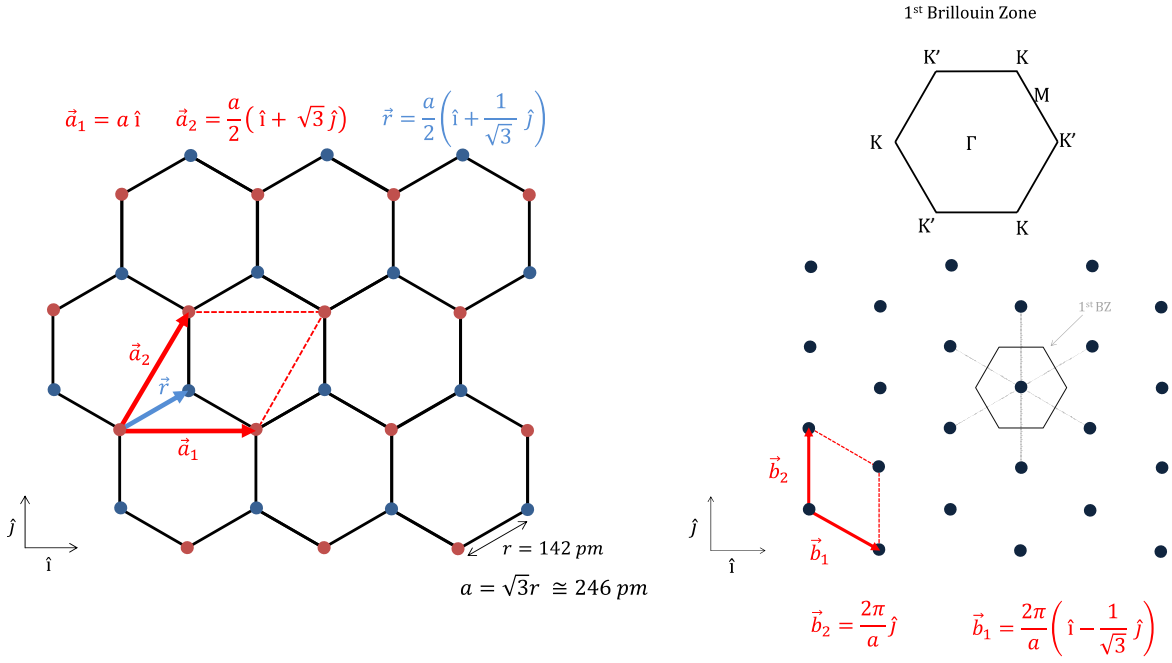

Figure 1. Graphene crystalline structure. Left, the real space hexagonal lattice with a 2-atom base. Right, reciprocal space lattice and 1st Brillouin zone.

The most exotic property of graphene is maybe its energy-momentum dispersion, $E(\vec{k})$ near the K and K' points minima (Figure 2). In this region, for energy levels below 1 eV, the energy dispersion is described as $E(\vec{k}) \approx \pm\hbar|\vec{k}|v_F$ (considering the origin of $\vec{k}$ at the K and K' points) forming the so called Dirac Cones [27, 29, 30]. With this particular linear dispersion, the electrons (and holes) behavior is analog to that of light ($E = pc = \hbar kc$), thus they are considered to behave like massless fermions. Furthermore, the conduction in graphene approaches the ballistic regime, where very low scattering occurs, leading to very high charge

carrier mobilities ($> 1.5 \times 10^4$ cm^2 V^{-1}s^{-1} , reaching 2.0×10^6 cm^2 V^{-1}s^{-1} in suspended graphene) [6, 10]. However, the band gap of graphene is null, hindering the implementation of graphene as the active material for logic switches, where its high mobility should end the reign of silicon. The absence of a band gap leads to relatively low on-off ratios in graphene devices, requiring high voltages (leading to high power consumption) to properly gate a logical transistor [26]. It is although possible to induce a band gap in graphene, either by doping, mechanical stress application or quantum confinement by producing graphene nano-ribbons (GNR) and nano-meshes (GNM)[31]. Nonetheless, band-gapless graphene has still room for high frequency RF applications [26, 32, 33].

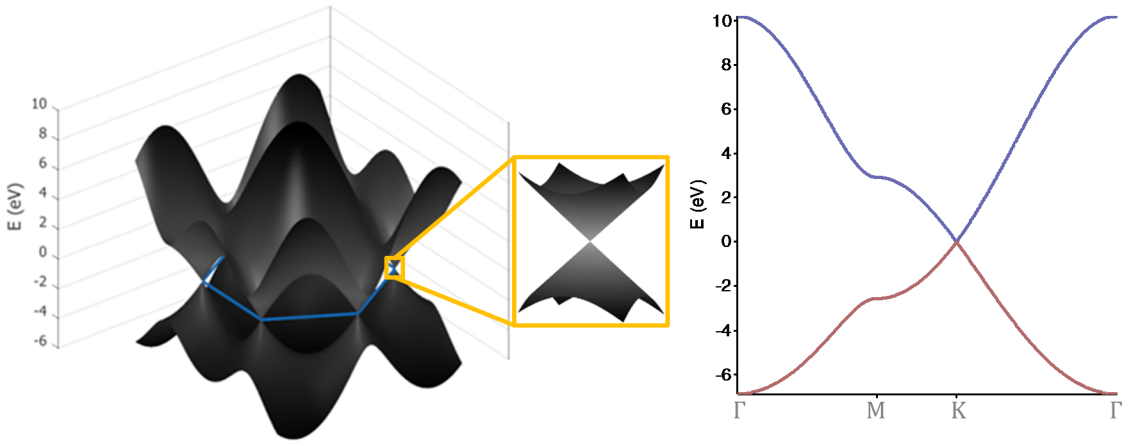

Figure 2. Graphene electronic energy dispersion. Left, 3D band structure with the first Brillouin zone identified by the blue hexagon. A detail at K-point, in inset, reveals the linear dispersion at the Dirac cones. Right, a cut along the Γ-M-K-Γ points of the band structure, again focusing on the linear dispersion at K. Plots done according the nearest-neighbors tight binding expressions found at [30].

Graphene is a broad band transparent material, having an optical transparency of 97.7 % [9]. This fact, associated with its excellent electrical conductivity, makes graphene a promising material for the replacement of Indium Tin Oxide (ITO) and other transparent oxides in transparent electronics [17]. The heat sinking ability of graphene would also be a plus in this matter [34].

Mechanical strength is another property of this wonder material. With a Young modulus of 1 TPa [8], graphene is the strongest known material, surpassed only theoretically by carbine [35] (which is actually explosive and shouldn't account for this matter at all). It was even demonstrated that multi-domain graphene sheets hold as much as 90 % of the single sheet strength [36].

Synthesis Methods

Many synthesis methods (Figure 3) have been developed since 2004 for the production of graphene, being some of those described in Table 1.

Table 1. Graphene synthesis techniques review.

Technique	Advantages	Disadvantages	
TCVD	-High-quality large area graphene on metal foils (mainly copper) -Scalable	-Requires a transfer process, reducing the quality in the target substrate	[15, 16] [37, 38]
MPCVD	-Faster when compared to TCVD -Has the potential for synthesis at lower temperatures	-Requires a transfer process, reducing the quality in the target substrate	[39] [40–43]
SiC reduction	-High quality epitaxial graphene	-Substrate price -Inefficient transfer process	[14]
Graphene oxides reduction	-High throughput -Suitable for functionalization	-Small flakes with decreased electrical and thermal properties	[19]
Mechanical Exfoliation	-Top quality graphene	-Very low throughput	[4]
Wet Exfoliation	-High throughput	-Small flakes	[18]
CNT unzipping	-Easy production of GNR with controlled sizes	-Low throughput	[44]
Direct laser synthesis	-Direct graphene patterning	-TCVD graphene has better properties even after the transfer process	[45]

TCVD on copper is showing to be the most viable technique for large scale production as roll-to-roll systems have already been developed, resulting in good quality monolayer graphene films on a polymer (Figure 3 D and E) [17]. Such graphene can be transferred onto an arbitrary substrate [46]. However, TCVD requires temperatures close to the melting temperature of copper (1083 °C) [47] and relatively long growth times. MPCVD could however change this [39]. While in TCVD the chemical species are activated by the high temperatures, MPCVD relies on the highly reactive radicals produced by the plasma. Those radicals will in turn react at the catalytic copper surface and form graphene. As the reagents activation is done much more efficiently by the plasma than by high temperature, plasma systems have the possibility to synthesize graphene at much lower temperatures and at faster rates [43], motivating the research in the MPCVD synthesis. MPCVD is also a technique suitable for the synthesis of graphite, CNTs and diamond, reason why it is the most interesting for the production of carbon hybrids [22, 48].

Applications that requires high volumes of material, such as polymer reinforcement, will not rely in CVD graphene. For those, reduced graphene oxides (r-GO) or wet exfoliated graphite (Figure 3 B) will be the obvious candidates due to their high throughput [18].

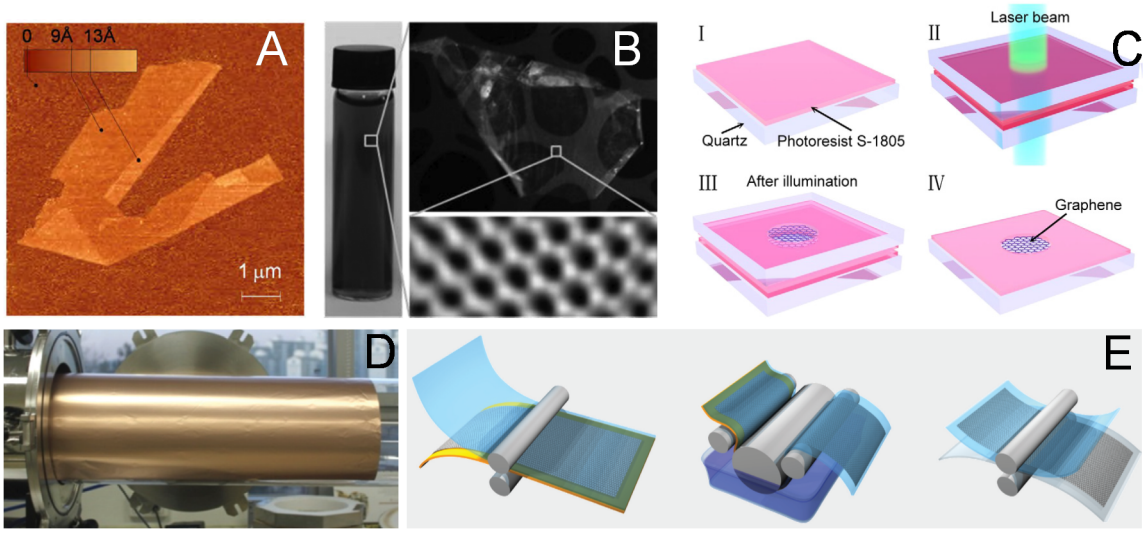

Figure 3. Various graphene synthesis methods. A – Mechanically exfoliated graphene AFM image. Despite the excellent properties of this type of graphene, only small flakes can be produced [10]. B – Wet exfoliated graphene. Small flakes with high throughput can be produced by this method [18]. C – Direct laser synthesis. Graphene can be produced and patterned at the same time [45]. D – Large area TCVD growth on copper foil [17]. E – Roll-to-roll graphene transfer process. It can be used along with continuous CVD synthesis for series production of graphene sheets [17].

Applications

A wide range of potential applications of graphene arises from its outstanding properties and peculiar dimensionality. A list of some of those follows:

- **Chemical and biological detectors:**

  Graphene field effect transistors have been extensively used as sensors for chemical species and biological markers, showing both high sensibility and differentiation (depending on functionalization) [49];

- **New photovoltaic devices:**

  Due to is high mobility which allows fast carrier recollection, reducing recombination events, graphene based and graphene enhanced photocells have been developed. Moreover, a carrier cascade generation effect has been observed and might be explored to further increase photocurrent [50, 51];

- **Broadband efficient photodetectors:**

  Graphene heterostructures comprising two layers have been demonstrated to work as a room temperature photodetector from visible to mid-infrared radiation [52];

- **Transparent electronics:**

  With only 2.3 % absorption in the visible spectrum while keeping an excellent electrical conductivity, graphene is a strong potential competitor to the conductive oxides such as ITO as a transparent electrode. Moreover, its mechanical properties allow its application in flexible electronics. Tactile screens have also been built using graphene [46, 53];

- **As a composite material:**

  Graphene can be used in composites as the reinforcement material, contributing to an overall increase in the material's strength and conductivity [18];

- **Active electronic components:**

  Graphene field effect transistors (GFET) for RF applications with increased bandwidth are one example where graphene can easily outperform silicon devices [24, 26, 32];

- **MEMS and NEMS:**

  The outstanding electromechanical properties of graphene will be of great interest in the development of new micro and nano-electromechanical systems (MEMS and NEMS), namely acoustoelectric transducers [54, 55];

- **Metrology:**

  The room temperature quantum hall effect of graphene, quantized by physical constants works as an intrinsic resistance standard, which can be used as a way to calibrate resistances [56];

- **Cold cathode emission:**

  Diverse reports exist where the field emission properties of graphene and graphene hybrids devices reveal to be suitable for cold cathode emitters [13, 20];

- **Filters:**

  Water filters based on graphene are proving to be game changers in the industry. An example is the research in desalinization filters [57];

- **Supercapacitors:**

  The high area to volume ratio and conduction properties of graphene makes it an excellent choice for high capacity, high current supercapacitors [12, 23].

Graphene Diamond Hybrids

Graphene Diamond Hybrids (GDH) have been studied since the rise of graphene in both theoretical and experimental works. Looking at the Table 2, it easily observed the similarities in thermal and mechanical properties of graphene and diamond. In fact, one of the main interests in joining these materials comes from this compatibility and their opposite electrical behavior, as diamond is a reference isolator while graphene the almost ideal conductor. The combination of both materials could be synergistic in fields like electronics where all-carbon devices might become a reality. However, the close interaction between both carbon allotropes might prove to be more relevant than their individual properties. In fact, this interaction might solve one of graphene limitations: the null band gap.

Table 2. Physical properties of graphene and diamond

	Graphene		**Diamond**	
Carriers mobility	15000 $cm^2\ V^{-1}\ s^{-1}$ (in substrate) 200000 $cm^2\ V^{-1}\ s^{-1}$ (suspended)	[6] [10]	4500 $cm^2\ V^{-1}\ s^{-1}$ (electron) 3800 $cm^2\ V^{-1}\ s^{-1}$ (hole)	[58]
Young modulus	1 TPa	[8]	1.2 TPa	[59]
Optical transparency	97,7 % (1 layer)	[9]	$\alpha < 1\ cm^{-1}$ ($\lambda > 235$ nm) [a]	[60]
Thermal conductivity	600 – 5000 $W\ K^{-1}\ m^{-1}$	[34]	2200 $W\ K^{-1}\ m^{-1}$	[61]
Band gap	Direct - 0 eV	[10]	Indirect - 5.47 eV	[60]

Opening a band gap would be of extreme importance for applications is switching electronics. In fact, it was shown by first-principle calculations that the interface between graphene and a diamond surface does indeed open a gap in graphene [25]. Some other computational study focused in how the outstanding thermal conductivity of both diamond and graphene could change the paradigm of efficient electronics [21]. Other study reveals that anisotropic conduction can arise from graphene-diamond interaction in certain configurations [62].

In the experimental panorama, earlier studies appeared about field emitters applications where graphene acts as a charge feeder and diamond as an emitter due to its negative electron affinity [13, 63].

The possibility of using diamond as a dielectric in graphene based devices was also explored in a study of the current carrying capacity of graphene-on-diamond. It was revealed a five-fold increased performance in the breakdown current, comparing to graphene on SiO_2 substrates

[a] α is the absorption coefficient and λ the wavelength.

[24]. Additionally, nano-diamond/reduced graphene oxide materials have been prepared exhibiting high specific capacitance, with obvious implication in supercapacitors [23]. Another recent work showed the interest in GDH's as lubricants [64].

Finally, a group has sprinkled fluorinated NCD over graphene, promoting the binding between NCD and graphene in high temperatures. The material produced by this procedure revealed a bottlenecked conduction caused by the percolating diamond clusters and exhibited a negative magnetoresistance [65].

Nevertheless, all those experimental reports were based on joining both allotropes grown by different processes, having no report been found on the simultaneous synthesis of GDH, the main finding in my bachelor thesis. These hybrids synthesized in a single run by MPCVD were the motivation for this work. Their morphology, as observed in Figure 4, was different from any other reported hybrid: nano-crystalline diamond (NCD) hemispheres sprinkled over a continuous graphene film.

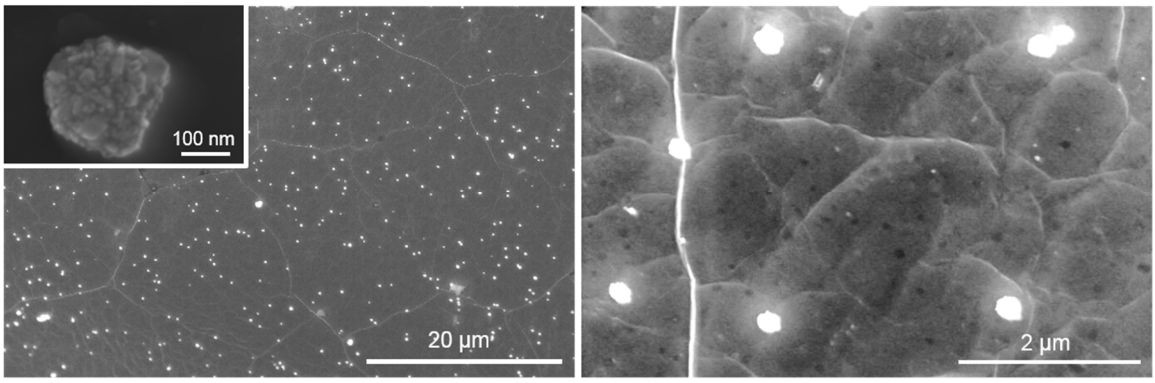

Figure 4. SEM images of the previous synthesized GDH. Left, wide view where the wrinkled graphene can be observed beneath the NCD clusters. Right, close look enhancing the wrinkled structure and the dark nucleation points. In inset, a detailed image of a NCD cluster.

Characterization Techniques

Raman Spectroscopy

Raman spectroscopy [66] has been described as the perfect technique for graphene characterization [67]. In fact, the quick and non-destructive analysis of this technique allows one to access important structural informations about graphene and other carbon allotropes due to their particular Raman signature. Raman spectroscopy is based in the inelastic light-matter interaction. When a given photon of energy $h\nu$ reaches a material, three kinds of scattering may occur: Rayleigh, Stokes and anti-Stokes. In the elastic Rayleigh scattering, the material is excited to higher virtual energy state and quickly decays to the starting energy level, emitting a photon of the same energy. In Stokes scattering, the decay occurs to the same starting electronic level but to a higher vibrational energy level, thus emitting a photon of energy $h\nu - q$. This energy difference q is compensated by the creation of a phonon with an energy equal to this difference. In anti-Stokes scattering the emitted photon has an energy of $h\nu + q$ as a phonon is annihilated in the process. In this case, the transition occurs to a lower vibrational state. This implies that the starting state is not the fundamental vibrational state, which reduces the probability of this kind of transitions. This transitions can occur by mean of a single phonon or by multiple phonons with or without the same energy. By measuring the frequency shifts of a laser illuminated sample, one can identify the energy of the phonons interacting with the incident photons. As the energy of the different phonon in a given material is a known intrinsic characteristic of the material, Raman spectroscopy can be used as both a structural and composition probe.

While pure diamond mainly shows a single narrow peak at 1332 cm^{-1} (Figure 5 C) [68], graphene spectrum is thankfully much more complex (Figure 5 A and B) [69]. This added complexity is what allows for the graphene characteristics to be assessed. From lower to higher energies, the first observed band is the D band[b] at ~1350 cm^{-1}, a band originated by a radial breathing mode of the aromatic rings (A_{1g} mode) [70]. This band is forbidden in perfect graphene due to selection rules. However this rules are relaxed in the graphene edges [70], presence of structural defects [69] or by the percolation of the lattice by sp^3 bonds with other species (for example hydrogenation)[71]. Also associated with defects, the D' band (~1620 cm^{-1}) follows with a low intensity. The intensity relation between the D and D' is reported to be an indicator of the type of defects [72].

The G band (~1580 cm^{-1}) is the distinct mark of sp^2 carbon and is present in graphite, nanotubes and graphene and is originated by the sp^2 bonds stretching (E_{2g} mode) [73].

[b] Unlike most Raman bands, this band is dispersive, i.e., the transition is dependent on the exiting wavelength. The given value is the typical for a 532 nm excitation.

At ~2450 cm^{-1} comes the D+D'', a mixed band of the D band with a weak transition at ~1084 cm^{-1} [74].

The most intense band in pure graphene, the 2D band, is the resonant second order of the D band. Unlike the D band, this band is allowed by selection rules, as 2 phonons with symmetric momentum are involved, thus fulfilling the $\Delta k = 0$ selection rule [67]. This band appears at ~2700 cm^{-1} and various reports in literature perform an analysis of the number of graphene layers based on its intensity and shape. In SLG, the 2D intensity reaches values up to four times that of the G band in monolayer graphene [69]. Multiple stacked layers of graphene interact in such a way that both D and 2D bands split (Figure 5 D). This splitting, besides a drop in intensity, originates a different spectra for different number of layers, being the 2D band FWHM and composition an indicator for the number of layers (Figure 5 D). However, this only happens in Bernal (AB) stacked graphene (Figure 5 F) [67, 75].

At ~2950 cm^{-1} the mixing of the D an D' bands is usually present in defective samples and finally, at ~3250 cm^{-1} the D' overtone, 2D', appears as a sharp small peak [67]. The band with highest energy is found at 4290 cm^{-1} and is the mixed mode 2D+G [74]. This band is seldom studied as poor information can be extracted from it and it is far from the "graphene fingerprint" region from 1100 cm^{-1} to 3300 cm^{-1}.

For multilayered samples, the C band (Figure 5 E) appear close to the excitation wavelength, at ~30-50 cm^{-1} [67]. This band, resulting from the interplanar tangential vibrations of graphene sheets, has a different Raman shift according to the number of layers, allowing their quantification.

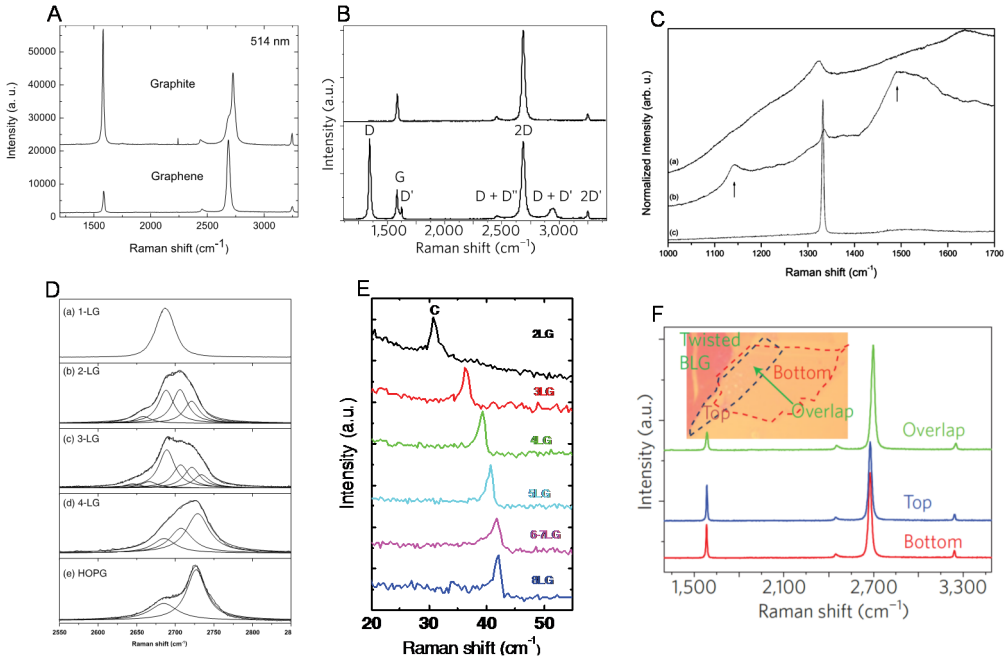

Figure 5. Raman Spectra of carbon materials. A – Graphite and graphene. B – Pristine (top) and defective graphene (lower). C – NCD with (mid) and without TPA (top) and bulk diamond (lower). D – D band splitting in Bernal stacked graphene multilayers. E – C modes blue shifting with the added number of layers. F – Non-Bernal stacked bi-layer graphene exhibiting single layer spectrum.

Optical Microscopy

Although a monoatomic material, graphene absorbs 2.3 % of the incident visible light per layer [9]. This allows us to observe and compare regions with different number of layers, either by transmission optical microscopy or by reflection microscopy of graphene over a 300 nm SiO_2 on Si (Figure 6 A and D) [76]. This substrate enhances the contrast by an interference phenomena and was the technique used by A. Geim and K. Novoselov when first identifying graphene [4].

Scanning Electron Microscopy (SEM)

SEM is one of the most interesting techniques for the study of micro and nanoscale materials as it provides a direct insight of a sample's morphology (Figure 6 C). Working in analogy to a reflection optical microscope, SEM bombards a sample spot with an electron beam. The interaction between the electron beam and the sample produces secondary electrons (alongside with other types of electrons) and X-rays. The mapping of the secondary electrons intensity reveals invaluable images for the morphological analysis of a material or structure. The produced characteristic X-rays can be used to perform Energy-dispersive X-ray spectroscopy EDS, thus allowing for the local elemental identification in a sample.

In the case graphene and carbon hybrids, EDS is not particularly interesting. SEM imaging is straightforward for diamond imaging, being the only problem the local charge accumulation in this insulator material (charge effect). However, graphene visualization is a more sensitive issue as a resolution-vs-contrast compromise has to be taken. High energy electron beams are used to gain resolution. With a higher speed, the beam divergence that occurs from electron-electron repulsion is reduced by the time it reaches the sample, thus reducing the spot size, increasing the resolution. Furthermore, higher energy electrons have a lower wavelength, reducing the diffraction limit at the sample, increasing the resolution. Reducing the beam's current would also reduce the spot size, but the required increase in the acquisition time turns the operation very hard and image acquisitions very long. However, by increasing the energy of the beam, the penetration depth of the electrons is increased. With a deeper range, the detected signal has a larger contribution from the substrate than from the thin graphene layer, thus reducing the contrast.

Transmission Electron Microscopy (TEM)

While SEM is analog to reflection microscopy, TEM is the electron microscopy equivalent of optical transmission microscopy. In this technique a very high energy electron beam penetrates trough a thin sample, being detected in a forward scattering configuration. The emitted electrons are deviated and absorbed by the sample, forming an image of beam intensity below the sample that is recorded by a 2D detector. Alternatively, a diffraction image can be made by setting the lenses for a diffraction configuration, from which structural parameters can be directly measured.

While for most samples the preparation for a TEM image is a hard and tedious process, as samples need to be polished until a sub micrometer thickness is achieved, for graphene this process is straightforward as the material intrinsically surpasses this experimental constrains. The main interest in TEM of graphene samples is the assessment of the number of layers (Figure 6 B).

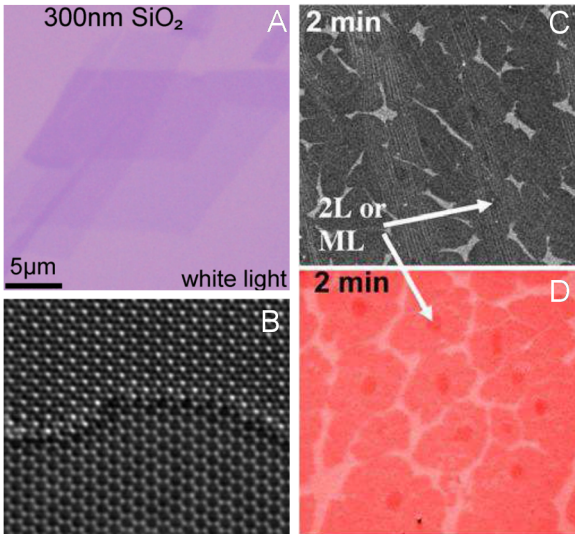

Figure 6. Optical and electronic micrographs of graphene. A – Optical image of a graphene flake over a 300 nm SiO_2 film for enhanced contrast [76]. B – TEM image of overlap between two layers (single layer below) [77]. C – SEM image of growing layer, with nucleation zones indicated [37]. D – A optical image in an enhanced contrast substrate of the same sample shown in C [37].

Atomic Force Microscopy (AFM) and Electrostatic Force Microscopy (EFM)

AFM is a microscopy technique based on the atomic electrostatic interaction between a very sharp tip of a cantilever and the sample. By measuring the force between the tip and the sample a topographic map can be made. Many modes of operation can be used, either by keeping the tip at a constant height or at a constant force, both in continuous contact or in tapping mode. Besides the force, the cantilever, similarly to a tuning fork, oscillates at a given resonant frequency and images can be generated by the phase shift this oscillation suffers from the interaction with the sample.

This technique has a sub-nanometer resolution and allows atmospheric pressure measurements to be made. It is also easily complemented with electric, magnetic or optical measurements with tips with different coatings.

In this work, a variant of AFM was used. EFM is an atomic microscopy technique where a potential is applied between the tip and the sample for enhanced contrast. It is also possible to make electrical properties measurements trough data analysis of scans at different bias voltages [78].

Electrical Characterization

From resistivity, for transparent contact production [46], to quantum Hall effect, for the study of the intrinsic properties of graphene and metrology [56], distinct electrical characterization techniques are applied to graphene and graphene hybrids. In this work a graphene field effect transistor was built in order to measure the carrier mobility of the samples.

In graphene the ambipolar field effect is originated by tweaking the Fermi level of the material [4]. By applying an electrical field to graphene, the Fermi level is changed following the potential. This effect will increase the density of states at the Fermi level, thus increasing the number of charge carriers. As a boost in the number of charge carriers increases the conductivity of a material ($\sigma = n\mu e$)[c], a variation in the applied voltage can be used to modulate the resistivity of the material. This is the operation principle of a graphene field effect transistor: a gate voltage is applied in order to modulate the drain-source current.

The typical transfer curve of a GFET near the conductance minimum, the Dirac point (V_{Dirac}), follows $I_{DS} = g_m|V - V_{\text{Dirac}}| + I_o$ with $V_{\text{Dirac}} = 0$ (Figure 7, left). However, due to the non-perfect lattice and the interaction with substrate and atmosphere, the derivative at V_{Dirac} is continuous. The position of V_{Dirac} itself is changed by the doping of the material: n-type graphene exhibits $V_{\text{Dirac}} < 0$ while p-type graphene has a $V_{\text{Dirac}} > 0$. The transconductance, $g_m = \frac{\partial I_{DS}}{\partial V_{GS}}\Big|_{V_{DS}=const}$ is the other interesting parameter that can be extracted from a transfer curve, as it can be used to calculate the mobility of graphene by

$$\mu = \frac{L g_m}{W C_g V_{DS}} \tag{1}$$

where L and W (Figure 7, right) are respectively the length and width of the channel, C_g the gate capacitance and V_{DS} the applied voltage between the gate and the source [26]. The transconductance is the same for the both electrons and holes conduction regimes in ideal graphene. Although sometimes this is not the case and electron and holes have different mobilities.

The gate capacitance can be estimated using a parallel plates capacitor model by $C_g = \frac{\varepsilon_r \varepsilon_0}{d_{ox}}$, being ε_r and ε_0 respectively the relative and vacuum electric permittivity and d_{ox} the gate oxide layer thickness.

[c] σ represents the conductivity, n the carriers concentration, μ the charier mobility and e the electron charge

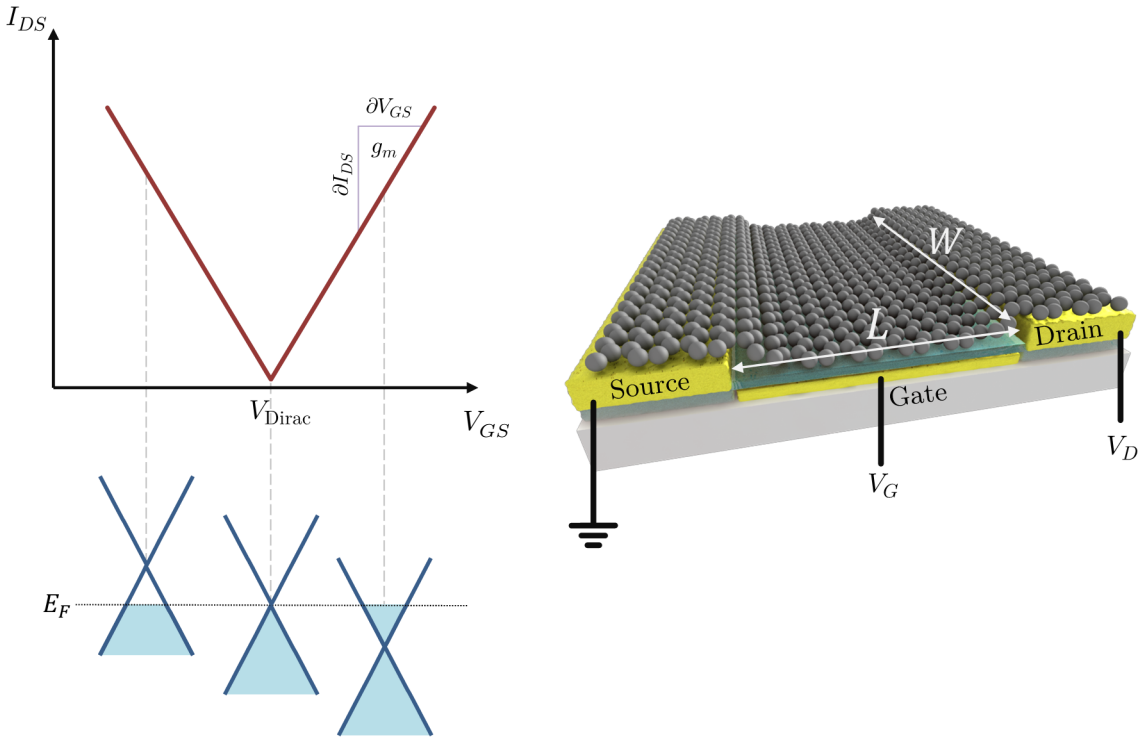

Figure 7. GFET schematic and operation principle. Left, ideal transfer curve. The change in the Fermi level by the potential application increases the number of holes/electrons available for conduction, thus modulating the conductivity. Right, schematic of a GFET active region. Graphene is laid on top of source and drain contact and a gate insulated by a thin dielectric. L and W, the length and width of the gate are identified.

Experimental

GDH Synthesis

Substrate preparation

The graphene diamond hybrid synthesis was carried on $10 \times 10 \times 1$ mm^3 substrates cut from commercial electrolytic copper plates. In their raw state, the plates exhibited a significant oxidation patina. Therefore, before the substrates cutting in a metal corner cutter, the plates were polished using a commercial metal polisher. After the cutting, the square substrates were sonicated in acetone for 15 minutes, to remove the polishing agent and the lubricant oil from the cutter. To remove acetone residues, an additional 15 minutes sonication in ethanol was performed. To hinder oxidation between the preparation process of the substrates and the MPCVD synthesis, the copper was stored in an ethanol bath inside a closed container.

MPCVD Synthesis

The hybrid synthesis was carried in an ASTeX AX 6350 6 kW 2.45 GHz MPCVD system (Figure 8). In this reactor a high-power microwave magnetron is coupled trough a rectangular profile waveguide and an antenna to a cylindrical growth chamber. Through a set of three screws in the waveguide, one can control this coupling and reach a standing wave condition inside the evacuated chamber where all the power is dissipated into the plasma (and partially in the sample in some cases). The plasma is generated by the high microwave EM field that ionizes the gas molecules inside the chamber generating free radicals that will react to form the film. The target substrate is held on a holder over a water cooled stage.

The synthesis process of graphene and GDH can be divided into three steps:

- **Annealing:** The system is started at low pressure hydrogen atmosphere and the magnetron is switched on. A ramp of pressure/microwave power is followed until the growth pressure and power conditions are met. Then, the samples is let at the H_2 plasma for heating up, promoting the grain growth of graphene, and for the reduction of any remaining oxide on the copper.
- **Growth:** The carbon precursor, methane, is mixed to the hydrogen at the chamber's gas input so the deposition can begin. These conditions are kept for the duration of the growth.
- **Cool down:** The methane input and the microwave power are switched off at the same time. Then the sample cools down following the system's thermal inertia until a low temperature to avoid the oxidation of the copper. When the holder temperature reaches 40 °C, the system is vented and the sample removed.

There are many variables in this system, being most of them interdependent. Therefore, finding the proper parameter window for the synthesis of a given material in this reactor is a hard task. An analysis of the different variables of the system follows:

Chamber atmosphere composition

Despite the single element nature of the carbon hybrids the stoichiometry of the reaction is very important, as multiple concurrent mechanisms are present during the synthesis process. The used gases were CH_4 and H_2. Methane is the carbon source for the deposition, so the more CH_4 in the chamber, the faster the reaction. Hydrogen has two main roles. First, it is used to initialize and stabilize the plasma, as the high proton mobility allows for a homogeneous energy transfer throughout the plasma. Secondly, H• radicals are known to etch sp^2 carbon bonds [79, 80], so hydrogen plays a major role in the control of sp^2 carbon deposition, favoring the sp^3 phases. The H_2/CH_4 flow ratio thus control the deposition/etching equilibrium of sp^2 carbon, indirectly tweaking the likelihood of sp^3 or sp^2 phases. Hydrogen is also used in the annealing phase as hydrogen plasmas are strong reducers, removing any remaining oxide layer in the copper surface [16]. Hydrogen does also have a key significance in dangling bond suppression by covalent binding with carbon, consequently hydrogenating the synthesized materials. The control of the atmosphere's composition is made indirectly by the gases flows, making the actual composition dependent on the reactor response time, a critical aspect in short growth runs, as it is the case of graphene growth.

Chamber total pressure

The total chamber pressure influences the growth in two ways. Firstly, it increases the plasma density, increasing the number of reactive species. Secondly it increases the sample's temperature as with higher pressures the thermal conductivity of the atmosphere is increased, thus enhancing the thermal coupling between the plasma and the sample. Although the pressure can be directly controlled by the system, it is tightly dependent on the microwave power. To sustain denser plasmas more power is required, so there is a given latitude of pressure values for a given microwave power, and vice versa.

Microwave Power

Microwave radiation is the plasma energy source and the only heat source in this system. Thus, controlling its power will have a direct effect on the plasma itself. Increasing the microwave power will increase the plasma temperature and density (pressure needs to be adjusted accordingly). This way, both sample temperature and gaseous species reactivity is increased. Although an increase in reactivity should increase the growth rate (assuming a growth condition is found by the atmosphere composition), if the plasma is produced in contact to the sample, which is the case, high power plasmas will contribute to a physical etch of the grown film. If this is not a problem for diamond, graphene, a single atomic layer, will definitely be affected by this phenomena. It is then required to operate

in relative low power conditions. However, the used reactor minimum safe operation power is in the order of the growth parameters found for graphene, thus microwave power is a variable with low range of possible values for this system. Besides, high temperatures are desired for the carbon superficial diffusion on the copper and for the annealing phase, where copper grain growth takes part, further reducing the possibility of low power operation [16].

Holders' setup

Since microwave power and pressure choices are bind to a limited set of possibilities, as discussed before, another variable had to be added to allow the high required temperatures to be reached. The standard molybdenum holder of the reactor revealed to uncouple too effectively the sample temperature to the plasma temperature. So, following the idea reported by A. Kumar *et al.* [39], a 3 mm thick zirconia ring was used as a thermal barrier, allowing higher temperatures to be reached. However, the temperature was still too low and increasing the zirconia thickness would introduce a very irregular shape inside the reactor, which would affect the power coupling to the chamber and hinder the plasma creation and control. Other solutions were studied including wider and thicker alumina and silicon nitride discs over the molybdenum holder and graphite and molybdenum rings under the holder.

Time

Growth and annealing time can be directly controlled by the system. Although short times are required for the growth of graphene, diamond requires longer synthesis times. The 3 minutes annealing revealed to be enough to pre-heat the sample and promote the desired copper grain growth. The time control of the growth was however varied from seconds to hours. In short growths, problems arise as the response time of the system, namely when concerning the input gases and pressure, have the order of magnitude of the process itself, affecting the control and reproducibility. The cool down time known to be critical in the growth of graphene on nickel, is rather irrelevant in copper substrates as the deposition doesn't rely on the superficial precipitation of the absorbed carbon but in the adsorption of the radicals at the copper surface and a radical cycloaddition mechanism [16].

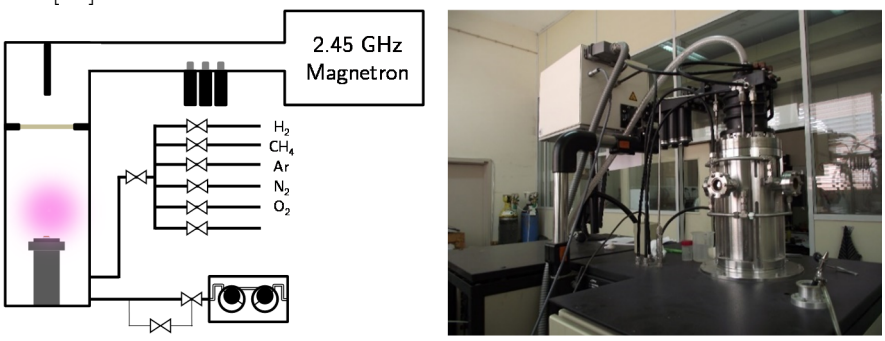

Figure 8. Used MPCDV reactor. Left, a schematic of the reactor, showing the growth chamber with cooled stage, the MW coupler, the magnetron, the gases input and vacuum system. Right, a reactor photo.

The search for a starting condition for which graphene and diamond could be simultaneously synthesized was thought to be unnecessary, as this work had been made by myself with reproducibility for over a year. However, for some yet unknown reason, the known parameters ceased to work, according to Raman taken from the new samples. The temperature readings in the stage seemed higher than usual so power was reduced. However, no positive results were found. Then a gas ratio search was carried out, as although no graphene was found, diamond clusters were. Methane concentration was increased in order to promote sp^2 bounding. Still no positive results were found. Although the higher temperature readings in the holder, by observing the samples it was perceived[d] that their temperature was lower than the usual. So an increase in power was conducted, with no success: diamond clusters were formed but still no sign of graphene. This meant that the temperature couldn't be increased by power as the physical etching was playing a major role.

A new approach was taken by changing the holder setup: instead of using only the zirconia ring to reduce the cooling in the samples, a 5 mm thick graphite ring was used under the molybdenum holder to further enhance the thermal uncoupling (Figure 9). Using this strategy and reducing the plasma power, it was possible to find a new set of parameters where graphene and diamond could be grown. In fact, this new operation window was more favorable for the growth of graphene as diamond clusters appeared with a lesser density than before. Another approach was also taken by increasing the pressure with results falling short of the expectations. In this approach, the gas flow for both gases had to be doubled for the system to be able to maintain the set-point pressure.

Four other holder setups were tested, one using an alumina (4 mm thick) disk instead of the zirconia ring, other using a SiN (6 mm thick) disks, a thin graphite disk suspended over the holder by 3 mm thick zirconia pieces and finally a molybdenum ring (5 mm thick) similar to the graphite one underneath the Mo holder (Figure 9). All the disks failed to be a good thermal insulator: contrarily to the zirconia ring, for the sample to reach the high synthesis temperatures (close to coppers fusion) very high power and pressures needed to be set (up to 1800 W and 70 Torr). In fact, the holders displayed a high temperature while the sample did not. This suggests that the heating of the sample comes mainly from induced currents in the conductive copper, dissipating energy through Joule effect. The disk holders displayed themselves as a flat surface "hiding" the sample to the MWs field. In the zirconia holder, the copper is prominent to the Mo holder and this shielding effect ceases. In fact, the dimension of the copper sample needs to be larger or the same size of the materials below as, with a wavelength of about 12 cm, the microwave radiation will be more easily induced in the larger holder plates.

[d] As the sample is thermally uncoupled to the cooled stage, the temperature readings of the system have little significance. As the plasma surrounds the sample a pyrometer cannot be used either. So, visual observation proves to be a good qualitative way to know if the temperature reached or not a desired level. For this, experience in the system is mandatory.

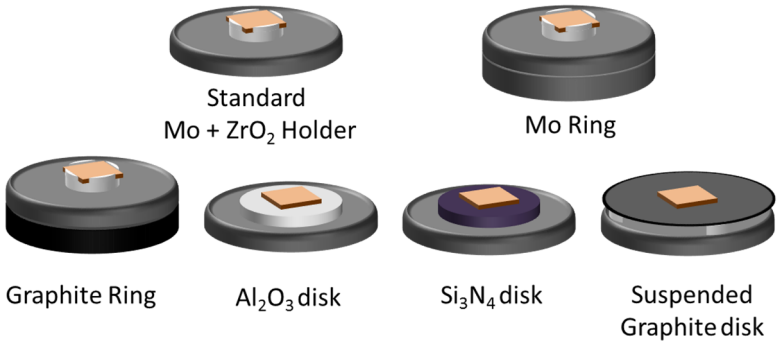

Figure 9. The various tested holder setups. All of the setups use a machined Mo disk with either a ring or a disk of different materials beneath or above.

Comparing the use of both rings, molybdenum has shown to be better as plasma arcs formed between the holder and the ring in the graphite one released carbon to the chamber, resulting in a lack of control of the stoichiometry of the reaction. However, contrary to the graphite one, the Mo ring also produced plasma arcs between the ring and the cooler. This behavior could damage the reactor if repeated, so it was decided to choose the graphite ring.

A baseline for the graphene synthesis was found at 1100 W, a 200 sccm of H_2 and 20 sccm of CH_4 gas flow at a total pressure of 27 Torr for 1 minute, after an annealing phase of 3 minutes in the same conditions but with no methane. After the reaction, the sample was cooled down in a 200 sccm H_2 flow to prevent the copper oxidation, which is enhanced for higher temperatures. A graphite ring under the molybdenum holder was used and the $10\times10\times1$ mm^3 copper sample was held over the latter by the 3 mm thick zirconia ring.

Having found a baseline from which to start, three strategies were followed to increase the diamond clusters density:

- **Increasing the growth time**

  It was previously observed that, when producing larger samples, it was necessary to increase the growth time in order to obtain a film all over the surface of the substrate. In this process it was spotted that the size and density of the clusters increased. Following this observation, some samples were produced for very long times, 1 and 2 hours with the goal of obtaining the maximum diamond density film over graphene.

- **Gas mixture change**

  As previously discussed, a larger hydrogen concentration will be favorable to the growth of sp^3 phases [79]. Thus a search in the gas mixture was conducted to enhance the diamond nucleation rate.

- **Diamond seeding**

  Diamond seeding is a well-known technique for the substrates preparation to enhance diamond nucleation in CVD growth on many substrates [80]. This seeding scratches

the surface leaving trace amounts of diamond inlaid on the substrate surface and promotes the development of defects at the surface. These diamonds and defects promote adhesion of the grown diamond film and serve as nucleation points. In order to seed the samples, they were immersed into a diamond powder (< 500 nm) suspension in isopropanol and sonicated for one and a half hour. After sonication, samples were cleaned in running ethanol to remove the excess diamond.

- **Phased growth**

  As growth time increase revealed to produce multiple layers of graphene, another strategy was followed to enhance the diamond nucleation. Instead of a single growth, several alternate phases where executed (Figure 10). There were two types of phases: The sp^2 phases, where CH_4 was added along H_2, and the sp^3 phases, where only hydrogen was injected into the chamber. This strategy was devised having in mind the effect of stoichiometry in the growth of different phases. In the sp^2 phase, the H_2:CH_4 is set to a value where graphene and NCD can simultaneously grow. In the sp^3 phase, methane is removed and a sp^2 etch is promoted, releasing carbon from the graphene onto the atmosphere, that given the high hydrogen content will deposit as sp^3 carbon, promoting diamond growth. By alternating between these phases, the formation of multiple graphene layers is hindered, while diamond formation is promoted.

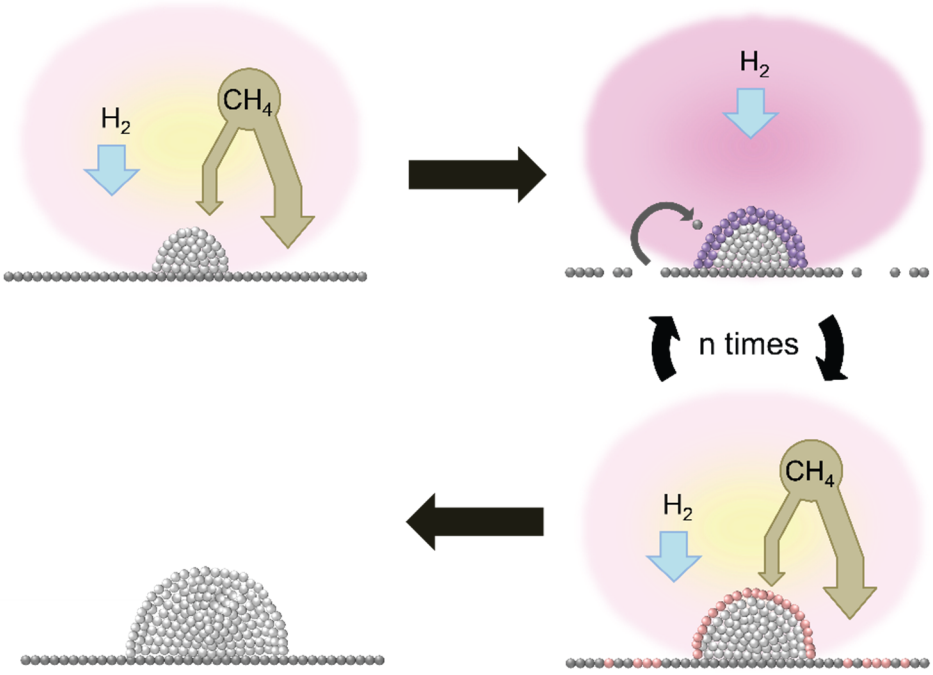

Figure 10. Phased growth schematic. The reaction starts with a sp^2 favorable gas mixture (H_2+CH_4). Then, periods with no methane are periodically executed in order to hinder multilayer formation and promote the sp^3 diamond phase. At the end, a higher diamond density is achieved.

The synthesis parameters for the samples from the nucleation control research are summarized in Appendix A (page 44).

GFET Production

In order to produce a GFET, first, a micro-fabricated substrate with drain and source contacts as well as a gate is required. To fulfill this task, a long process was taken inside a cleanroom involving various microfabrication techniques:

Photolithography

In order to pattern a device onto a surface, the design of that device must be somehow transferred to the said surface, either by removing material or adding material. To control the regions where the material is added or removed, a mask must be deposited to protect the regions that shall not be affected by the deposition/etching processes. To create this mask a photosensitive polymer (photoresist) is deposited onto the target surface and then exposed to UV radiation. Depending on the type of the photoresist (PR), either positive or negative, the exposed region is removed or kept, accordingly, during a revelation step where the hard polymer stays in the surface and the soft remaining parts are washed away.

In the semiconductor industry, the exposure is usually done by the light of an UV lamp modulated by a physical metallic mask, with or without projection systems. In this work however, a direct laser writing (DWL) system was used. In this system a physical mask is not required as the exposure is done by moving the sample in a XYZ table under a focused laser spot. Although its high versatility when compared to a conventional projection setup, the exposure time for a 20 cm wafer scales from a few seconds exposure to several hours, rendering the DWL only suitable for prototyping, small scale production or the production of the physical masks for high throughput exposure systems.

In this work, a Heidelberg DWL 2000 was used to pattern a 500 nm spin-coated layer of a cured AZ 1505 positive PR. After the exposure the PR was revealed using the AZ 400k developer. All the PR associated processes, deposition, cure and revelation, were carried in a Karl SUSS Gamma Cluster track-stepper.

Before the PR deposition, the wafer was submitted to a Vapor Prime process where hexamethyldisilazane was grown on the surface to improve the adhesion to the PR.

Deposition

Various techniques for deposition exist, such as CVD, atomic layer deposition (ALD), molecular beam epitaxy (MBE), electroplating, sputtering and others. In the GFET substrates production, all the depositions were done by sputtering. In this process argon ions are accelerated against a target of the to-be deposited material. Those ions promote the physical etching of the target, being the removed material projected to the substrate, being therefore deposited. Oxides and other alloys can be formed by using multiple targets and/or adding some elements in the gaseous phase, such as oxygen for oxides depositions.

In this work two sputtering machines were used, a Kenosystec multi-target sputtering system and a Singulus Timaris multi-target sputtering system. The Kenosystec was used to deposit the gold and chromium while the Timaris for the deposition of Al_2O_3 and TiWN.

Etching

Various etching processes exist from highly selective but strongly isotropic chemical etchings to highly anisotropic but poorly selective physical etchings. Reactive ion etching is a technique that joins the best from both chemical and physical etching, anisotropy and selectivity, although it was not used in this work.

Physical etching was carried at a Nordiko 7500 broad beam ion milling system with secondary ion mass spectroscopy end point detection. This machine used an argon beam accelerated against the substrate in order to remove material from it. The system is similar to a sputtering system but with the substrate in the place of the target. As the process is poorly selective, a mass spectrometer is used to control the concentration of etched ions in the etching chamber's atmosphere, being a reduction in their concentration an indicator of the end of a layer.

Wet etching was carried using the AZ 400k developer as its high basicity is suitable for the wet etching of alumina. Although this process could be done by simply using a regular strong base such as NaOH, the automatic control in the time and reagent quantities in the revelation track-stepper turned the use of this reagent a more practical solution to perform the etching.

Plasma etching is a special case of physical etching where the sample is immersed by the plasma, leading to a higher isotropy of the process. It is generally used to clean photoresist residues after a process. In this work a PVA Tepla GIGAbatch 360M plasma etcher was used to pattern graphene by the mean of an oxygen plasma.

Resist removal and cleaning

Depending on the chosen process, different removal procedures had to be followed. Using the patterning of a gold contact as an example, two strategies can be adopted: physical or chemical etching, preceded by gold deposition and PR pattern over the gold layer, or by the gold deposition on top of the previously patterned PR.

In the first case, after the process, the PR layer needs to be washed away. For this, the wafer is placed onto a solvent bath in ultrasounds at 60 °C for increased solubility. This solvent will remove all the PR. Acetone can be used for a wet etched sample, whilst for samples subjected to the ion milling beam a stronger solvent (Fujifilm Microstrip 3001) need to be used as the etching process hardens the PR layer.

If gold is deposited over the PR, when the solvent removes the PR, the covering gold layer, now without a substrate, is removed by the ultrasounds leaving the gold only in the regions where there was no PR. This process is called liftoff and exhibits the advantage of removing an etching step in the process. Besides from saving the etch process time, it avoids problems related to the etching selectivity. However, the edges of the liftoff patterned regions are rather

irregular, while in the ion milling process their profile can be controlled by the incidence angle of the ion beam.

Transfer

The direct graphene deposition on a target substrate is still a challenge. So, different transfer methods have been developed in order to place graphene where it is necessary. Most of these methods have in common the previous deposition of a support polymer layer, usually Poly(methyl methacrylate) (PMMA) [46]. After the deposition of the polymer, the catalytic substrate used in the graphene synthesis is either separated from the graphene or chemically dissolved. In the case of graphene on copper, if the chemical route is followed, the most common etchant is $FeCl_3$ [53]. The problem in using this process is that the polymer/graphene film is contaminated by the etchant, and chemical graphene doping may occur. As an alternative, physical peeling processes of the film from the copper are being reported [81].

In this work, the electrolysis assisted peeling was explored (Figure 11). After the PMMA spin-coating and respective cure at 180 °C for 15 minutes (Figure 11-I), the sample is placed in a vacuum holder with a back contact designed for the purpose. Then, the fixed sample is immersed into a saturated NaCl solution along with a graphite electrode. Afterwards, a 12 V potential is applied between the graphite electrode and the grounded cooper. As the contact on the copper is insulated from the electrolyte, all the current passes through the copper/graphene and the graphite, promoting the formation of hydrogen at the copper electrode. The hydrogen bubbles formed in between the copper and the graphene/PMMA film will then start to gently separate the graphene from the copper (Figure 11-II), ending up in a graphene/PMMA film floating on the water. The film is then collected by a thin metallic net and dried at room temperature. The dry film can be stored for later use. To complete the transfer process, a deionized water drop is placed on the target transfer region. After checking the graphene side with an ohmmeter, the graphene/PMMA film is dropped with the graphene downwards onto the water drop. Water surface tension holds the film in place. With the help of absorbent paper, most of the water is gently removed by capilarity. Then, with the help of a gas flow, the film is stretched over the target surface, serving the remaining water as lubricant in this process, hindering the formation of bubbles between the substrate and the graphene. After that, the sample is heated at 180 °C for 15 minutes to evaporate the remaining water and to promote the adhesion of the graphene to the substrate (Figure 11-III). Finally, the sample is immersed in acetone for 12 hours to dissolve the PMMA leaving only the graphene on the target substrate(Figure 11-IV). To improve this process, an airbrush can be used to keep a continuous acetone flow on the sample before and after this bath. After this bath, the sample is cleaned in anhydrous isopropanol (IPA) using the same spray/bath/spray process to remove acetone residues (the IPA bath only takes 1 minute). The transfer process is then complete (Figure 11-V).

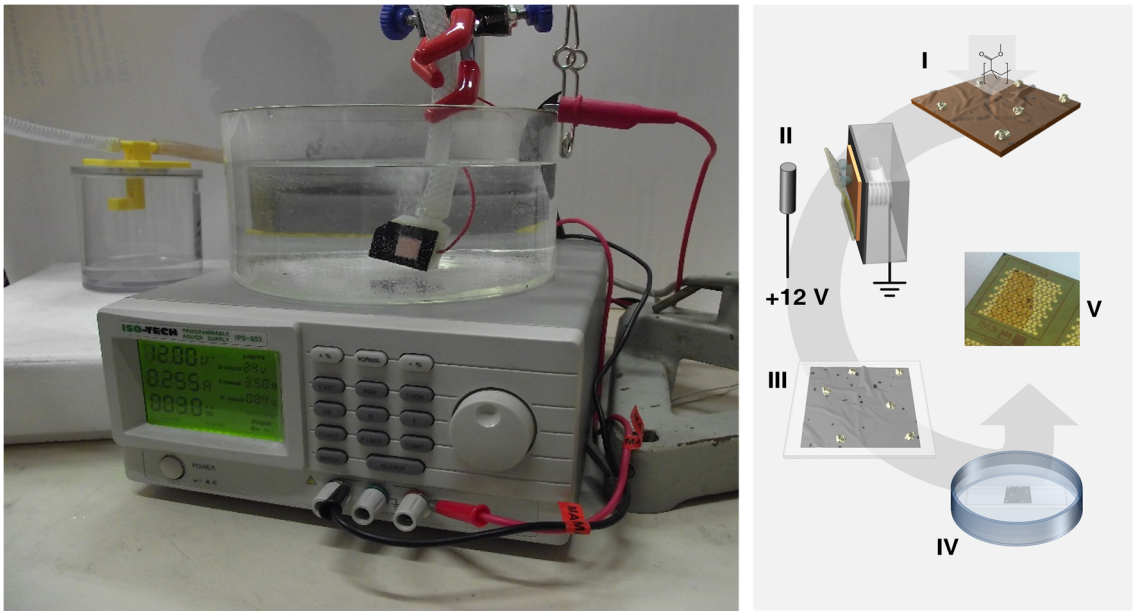

Figure 11. Transfer setup and process. Left, the setup with the 12 V power source feeding the electrolysis setup in a supersaturated NaCl solution above. The graphene on copper samples is held by vacuum and contact is made by a spring behind the sample. A water trap is used for safeguarding the pump. Right, a schematic of the process: I – PMMA is spin coated onto graphene and cured; II – Graphene/PMMA is peeled from the copper by electrolysis induced bubbling; III –the film is transferred over a target substrate and heated to promote adhesion; IV – PMMA is removed in an acetone bath for 12 hours; V – Finally graphene is obtained on the substrate.

Before starting the microfabrication, the design of the die architecture was produced using a CAD software. The chosen design consisted in four 66 transistor matrixes set in a 2×2 layout. Each transistor was composed by an individual bottom gate and its contact pad for measurements, sided by a drain and source contact, forming a 25 µm long and a 75 µm wide channel. Consecutive transistor rows were flipped 180° to take advantage of the triangular geometry of each transistor, thus increasing the number of devices per die. A step-by-step plan for the microfabrication process was defined at the same time (Figure 12). Next, the actual followed fabrication procedure is described, after adjustments due to some setbacks:

1. Wafer:

To begin the process a 20 cm diameter silicon wafer with a 200 nm thermal SiO_2 layer was chosen.

2. Bottom gate:

A 50 nm TiWN layer was sputtered all over the wafer to form the bottom gate conductor. Afterwards, PR was deposited, exposed and revealed[e]. The wafer was then ion milled to pattern the conductors. Finally the resist was removed and the wafer cleaned with IPA and ultrapure water. The die frames, symbols and alignment marks were also created in this step.

[e] From now on, this set of steps will be called “PR mask deposition”.

Afterwards, the height profile of the channel was measured using a profilometer, revealing a 110 nm step. This observation revealed that the ion milling etched into the SiO_2 layer.

3. Gate oxide and access vias:

A 30 nm alumina oxide layer was sputtered all over the sample. Then a PR mask was deposited to protect all the alumina except for the contact spots of the gate. Those exposed regions where subjected to a wet etching process to remove the alumina. The PR was removed and the samples cleaned.

4. Alignment marks protection and gold deposition:

The next deposited material was gold. Since gold is not transparent, it would optically hide the alignment marks created in step 2, rendering impossible further alignments. To avoid this, a PR mask was created to protect those marks. Afterwards, a 3 nm chromium layer was deposited to promote the adhesion between the substrate and the gold layer. Instead of the planned 30 nm gold layer, a 90 nm gold film was deposited to overcome the problem detected in step 2. To reveal again the alignment marks, the wafer was subjected to a liftoff process, removing the PR and the gold over it.

5. Drain source patterning:

A PR mask was formed and the wafer was ion-milled to pattern the golden drain, source and gate contacts. However, the ion-milling process went wrong and the alumina was also etched. Further steps had to be executed in order to create a new gate dieletric.

6. Alumina re-deposition and etching:

Step 3 was repeated with some changes. Now, besides only etching the alumina over the gate access areas, the drain and source contacts regions were also etched. However, at the end of the process, the profilometer revealed that a small misalignment led to the etching of a tiny stripe over the gate near the source contact. The alumina was then removed from the sample by another wet-etching.

7. Second alumina re-deposition and etching:

Step 6 was repeated, now using a different mask overlapping the contacts by a few micrometers to avoid further problems due to bad alignments. The process revealed to be effective and the substrates were finally ready for the GDH transfer.

8. Dicing and GDH transfer and patterning:

The individual dies were diced and the GDH was transferred onto the patterned substrates. A PR mask was deposited over the graphene, drain, source and gate contact, in order to etch the graphene to the size of the channel and protect the gold contacts from the plasma. However, after three etching runs, the degradation of graphene was far under the expectations, turning this method inadequate for the GDH samples. An alternative was found: with

mechanical etching, using a micro positioner with a sharp tip, it was possible to insulate graphene over only one gate, allowing the operation of the GFET. Having this method shown good results, it was adopted for both already plasma etched samples and samples with no other kind of etching.

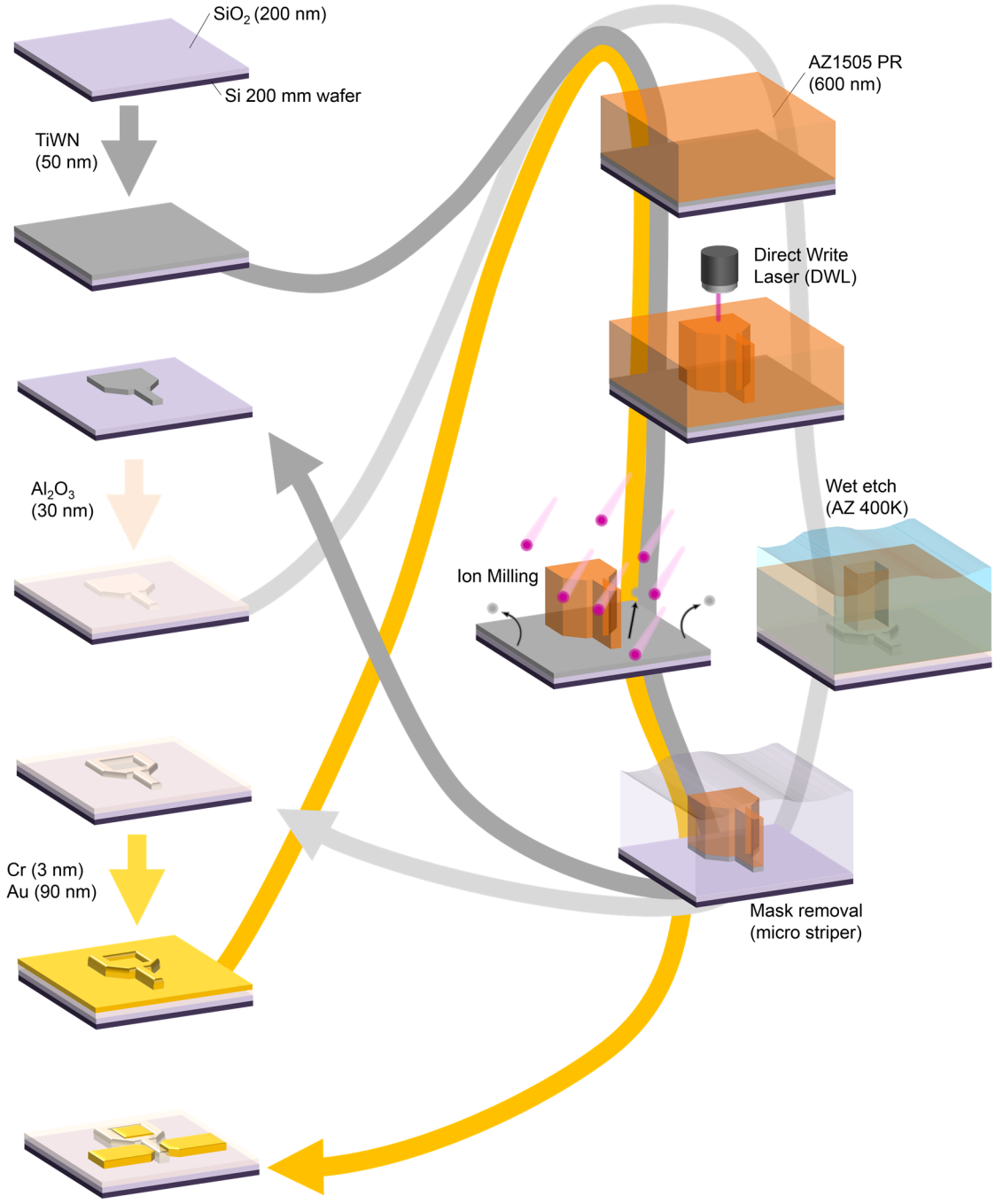

Figure 12. Planned microfabrication process: TiWN sputtering deposition flowed by a lithography step to form the gate; Al_2O_3 sputtering followed by a lithography step to remove the alumina from the gate contact; gold sputtering deposition and lithography for the formation of the drain and source, and to cover the gate contact. The procedure had an extra lithography step before gold deposition to protect the alignment marks from being covered.

Characterization

The Raman analysis was conducted in the backscattering configuration on a Jobin Yvon HR800 instrument (Horiba, Japan), using 1800 lines/mm grating and three different laser lines: a 532 nm laser line from a Nd:YAG DPSS laser (Ventus, Laser Quantum, U.K.), a 633 nm line from a Melles Griot HeNe laser, and a 442 nm line from a HeCd laser (Kimmon, Japan). An edge filter for each wavelength was used to filter the Rayleigh dispersion allowing Raman acquisition from 50 cm^{-1}. A 100× objective (spot size ~ 2 µm, 0.9 numeric aperture, Olympus, Japan) was used to focus the laser light onto the sample and to collect the backscattered Raman radiation to be detected by a Peltier cooled (223 K) CCD sensor. The spectrometer was operated in the confocal mode, setting the iris to 300 µm. AFM assisted Raman imaging was carried in a NT-MDT NTEGRA with a 473 nm excitation. UV-Vis transmittance measurements were carried out on a Shimadzu 3600UV.

TEM observations were carried in a JEOL JEM-2200FS microscope at 200 kV in bright field mode with the samples transferred to a copper grid (400 mesh). Scanning electron microscopy (SEM) was performed with a TECAN VEGA3 in secondary electron imaging mode. EFM measurements were performed in a Nanoscope IIIa Multimode. Besides topography measurements, EFM phase shift images, used to calculate the capacitive contribution and the electrostatic potential of the surface, were acquired in lift mode scan with a fixed tip-sample distance of 20 nm. Eleven scans were recorded for the different bias voltages applied to the surface from −5 V to 5 V with steps of 1 V.

Cleanroom processes were monitored using a KLA TENCOR P-16+ profilometer, a NovaNanoSEM 650 microscope with EDS, a Nikon Eclipse 2000N microscope and a Witec Alpha 300R confocal Raman

GFET characterization was done by measuring the drain-source current while sweeping the gate-source voltage. The drain-source voltage was kept constant in each measurement. A Keithley 2410 was used to control the gate-source voltage and leakage current while a Keithley 6487 was responsible for both drain-source bias and the drain-source current measurement (Figure 13). The contacts with the device were performed using thin tungsten tips controlled by manual micro-positioners.

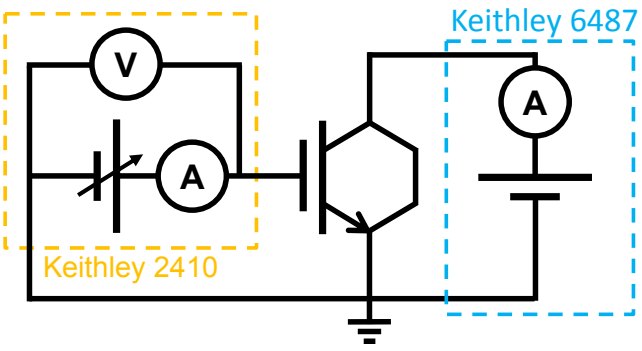

Figure 13. GFET test circuit. V_{DS} was kept constant and I_{DS} was measured by the Keithley 6487, while V_{GS} was varied by the Keithley 2410. GFET symbol as seen in [82].

Results and Discussion

GDH characteristics

To start, an analysis of the base hybrid material, the graphene layer sprinkled by NCD clusters, is performed.

SEM micrographs reveal the hybrid morphology (Figure 14): a continuous wrinkled film over the copper substrate sprinkled with ~200 nm bright clusters. The clusters display their polycrystalline nature at higher magnifications (Figure 14, right). The observed contrast of the clusters is due to local charge effect, resulting from their insulating nature.

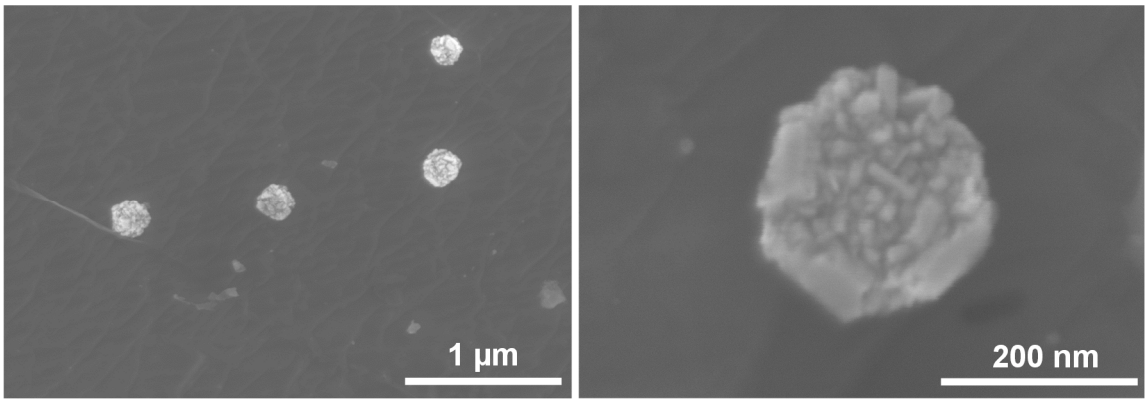

Figure 14. SEM micrographs of the GDH produced by the found baseline conditions. Left, a 35000× view, showing the clusters and a graphene wrinkle. Right, a NCD cluster close look, exhibiting its polycrystalline nature. Contrast is produced by charge effect.

In order to confirm the nature of the different phases of the hybrid, micro-Raman Spectroscopy was carried out both in a region without clusters and at a highly nucleated zone. The no-clusters region reveals a typical monolayer graphene Raman spectrum (Figure 15, green) with a very narrow and intense 2D band ($2D_{FWHM}$ ~ 26 cm^{-1}), featuring a I_{2D}/I_G ratio of ~ 4. The defect allowed D band exhibits however a strong contribution, with a I_G/I_D ratio of ~1.3, suggesting defective graphene [69]. Nevertheless, this observation is opposed to the D_{FWHM} of 18 cm^{-1}, a very low value for defective samples as defects scattering should produce a broadening of the bands. Hydrogenation, either total, forming the so called graphene, or partial, is described to produce samples with Raman spectra similar to those obtained [71]. As the synthesis and cool-down take place in a highly hydrogen rich atmosphere, typical of MPCVD, it would be more than natural that the obtained samples should be hydrogenated, specially when considering the high throughput of H• by the plasma [80].

The Raman spectrum of a highly nucleated region (Figure 15, red) revealed the typical NCD Raman signature, featuring wide and intense D and G bands revealing a strong contribution of the inter-granular amorphous sp^2 carbon. The trans-polyacetylene (TPA) bands at 1140 cm^{-1} and 1480 cm^{-1} are also typical of the NCD phase [68]. The diamond band at

1332 cm^{-1} appears very close to the D band for the 532 nm excitation wavelength rendering it hard to identify. However, for the 442 nm blue line, the D band shifts to higher energies and the diamond band is thus resolved. The 2D band however is still present as the laser spot is much larger than the clusters size and will inevitably measure the surrounding graphene spectra.

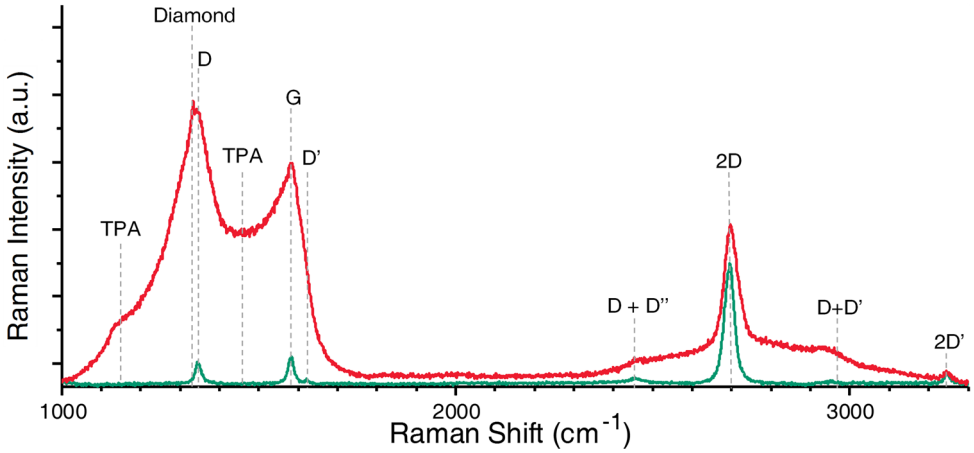

Figure 15. Micro-Raman (532 nm) spectra of the inter-cluster graphene regions (green) and of a region with very high NCD nucleation (red). All the bands are identified. The presence of the 2D band in the NCD spectrum is a consequence of the small size of the clusters (200 nm) when compared to the laser spot size (2 µm).

To obtain a spatial distribution of the clusters, and to prove the continuity of the graphene film, AFM assisted Raman mapping was performed (Figure 16). A map of the intensity of the 1332 cm^{-1} channel was overlapped over an AFM topographic image. A high correlation is observed between the Raman mapping and the topographic protuberances, confirming their nature as NCD clusters. Maps of the I_G/I_D reveal that the defects/hydrogenation is present all over the samples [72], while I_{2D}/I_G ratio suggests a single to bi-layer graphene over all the sample [69]. However, care must be taken when using the I_{2D}/I_G ratio as it is done throughout the literature. In fact, the typical D and 2D band splitting due to interlayer interactions, which contribute for those bands broadening and intensity drop, has shown to be dependent on the layers stacking. Bernal stacked graphene layers do in fact obey those band splitting rules, while randomly oriented stacked layers (incommensurable graphene) seem to be electronically uncoupled and their Raman spectra shape is not affected by the multilayer presence [67, 75]. Hydrogenation of multilayers can also be of relevance as inter-planar hydrogen will change the inter-layer interaction.

In fact, a study was carried out with sample I_{23} (Appendix A), a sample with almost no diamond clusters, which suggested a multilayer nature of the produced films. The sample was transferred to a transparent quartz substrate and a region was found where graphene had folded onto itself during the transfer process. A Raman spectrum was acquired in regions with different number of layers. The resulting spectra, as shown in Figure 17, revealed a typical

monolayer signature in all the regions, with variations of the I_{2D}/I_G ratio not correlated with the number of layers, as the supposed bilayer exhibited a higher ratio.

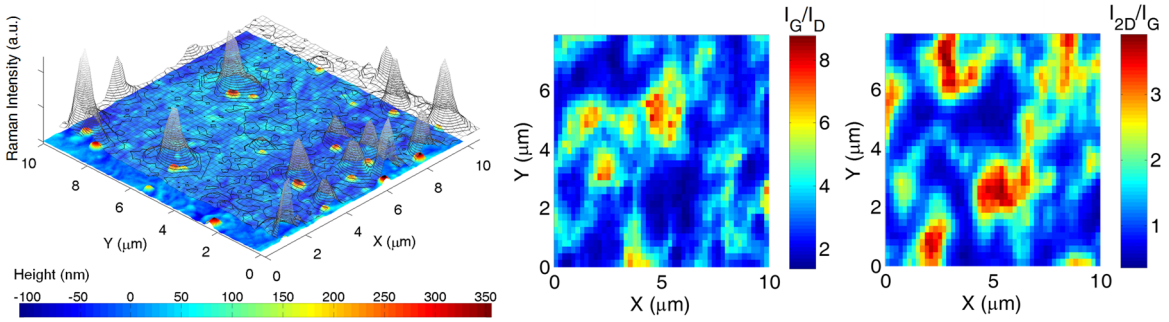

Figure 16. AFM assisted Raman mapping (473 nm). Left, 3D contour plot of the 1332 cm^{-1} diamond band over a AFM topography map. High correlation is found between both maps. Right, intensity maps of the I_G/I_D and I_{2D}/I_G ratios. The relatively low I_G/I_D found in most of the sample reveals the presence of defects, while the high I_{2D}/I_G ratio suggests the presence of mostly bi and single layer graphene.

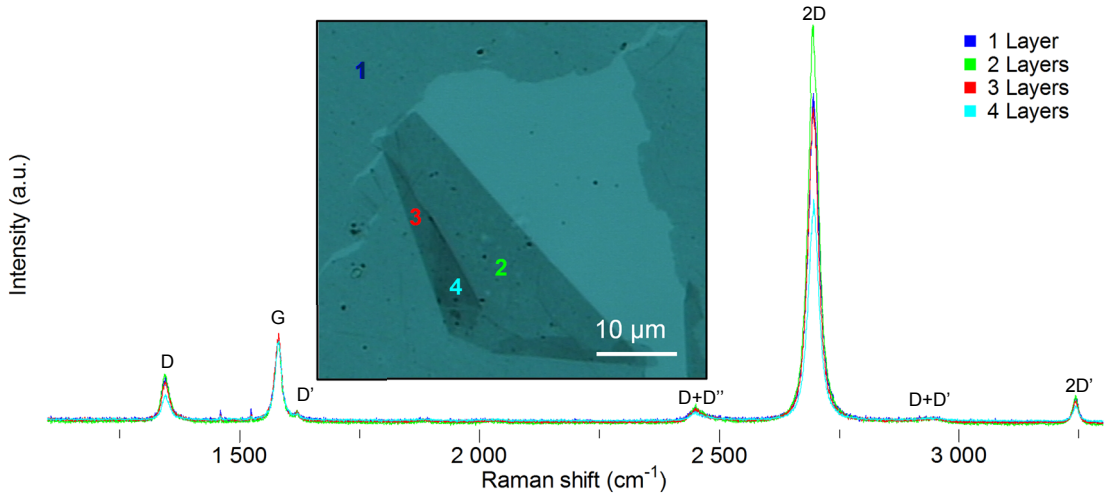

Figure 17. Micro-Raman (532 nm) spectra of folded graphene in quartz. The absence of differences between the spectra shows that multilayer graphene can exhibit a SL spectrum. This observations raises doubts whether the film is actually a single layer or not.

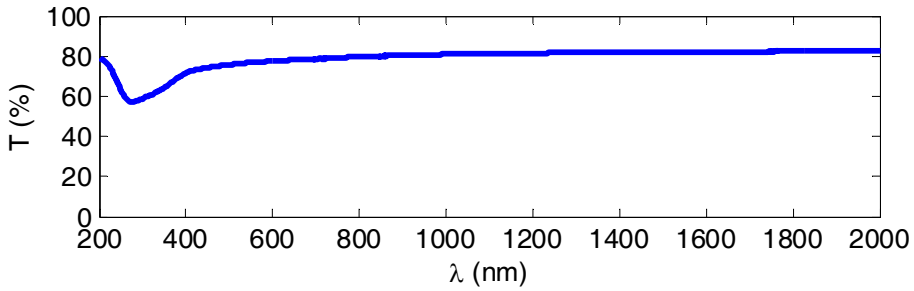

Figure 18. Transmittance spectrum of a graphene sample on quartz (corrected to the quartz reference). The response is flat all over the spectra, only with a $\pi - \pi^*$ transition at 270 nm [42]. The mean observed transmittance is ~80 %, suggesting the presence of 9 layers.

Furthermore, all the samples, including the ones with a very low amount of NCD, exhibited a significant visible light absorbance, noticeable by naked eye, in contrast to the 2.3 % expected for single layer graphene [9]. A UV-IR transmittance measurement (Figure 18) was carried out revealing an average transmittance of ~80 %, a result not compatible with single-layer graphene. Instead, this finding suggests that the measured film had up to 9 layers of graphene.

TEM micrographs (Figure 19) revealed the hemispherical nature of the clusters as well as their polycrystallinity and the presence of amorphous material at the inter-granular regions. The film appears sprinkled with small darker regions. These regions are typical of CVD graphene and represent nucleation sites where more layers do form [37]. It is possible to confirm the presence of diamond by the observation of atomic planes with a interplanar distance of 1.989 Å corresponding to the (111) plane of diamond. It was also found that in fact graphene had more than one layer, having a few layer basal planes with a 3.305 Å interplanar distance been observed. The connection between graphene and diamond is also hinted in TEM images. In the inset of Figure 19, the base of a cluster with a set of planes forming perpendicularly to the end of a (111) diamond plane is observed. This type of epitaxiality has been already suggested in the literature [73] and points to a covalent interaction between the two phases, explaining how the connection was kept after the strong sonication during the transfer process to the TEM grids.

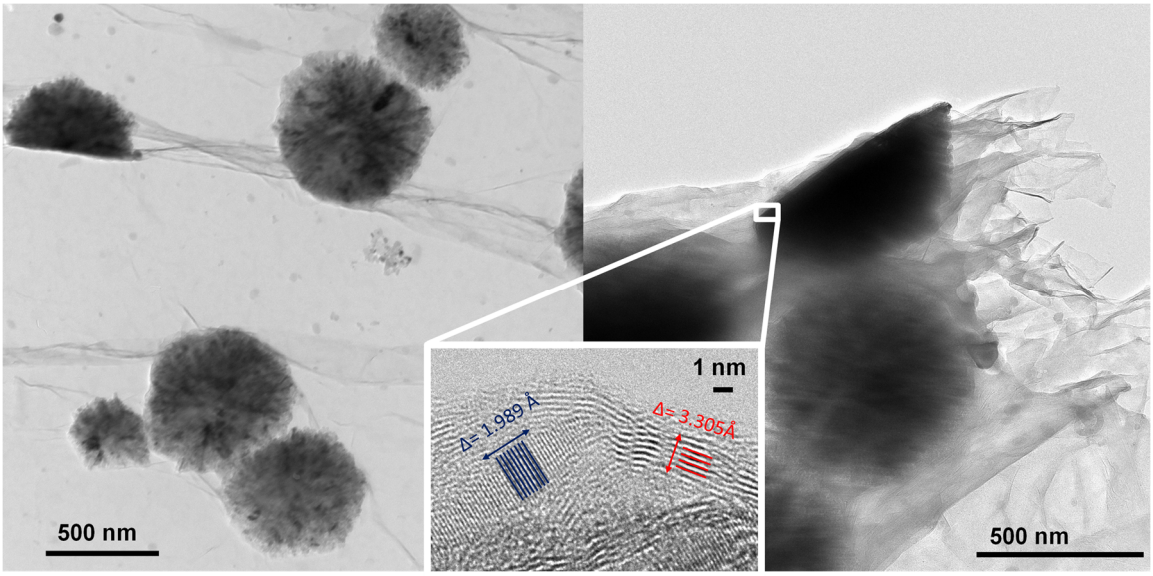

Figure 19. TEM micrographs of the GDH hybrids. Left, clusters can be seen on graphene, along with the multilayer nucleation spots. The hemispherical nature of the clusters is revealed. Right, close up of a cluster's aggregate wrapped by the graphene as a consequence of the transfer process. In inset, a high magnification image of a cluster's base, showing the transition from a (111) diamond crystal (blue) to a multilayer graphene (red).

Maps of EFM/AFM taken from a single cluster and its surrounding are shown in Figure 20. In the topographic image (Figure 20, left) we can again observe the multi-granular nature of the clusters. In the right image of Figure 20 the α parameter is mapped. This parameter is

obtained by fitting the tip phase shift ($\Delta\varphi$) for each point and each different bias voltage between the sample and the tip (V_{bias}) to $\Delta\varphi = -\alpha(V_{bias} - V_{CPD})^2$, where V_{CPD} denotes the tip-sample contact potential difference and $\alpha = -\frac{Q}{2k}\frac{\partial^2 C}{\partial z^2}$, being Q and k respectively the quality factor and elastic constant of the cantilever, C the local capacitance and z the tip-sample distance [78]. By assuming a naïve parallel plate model, we find that $\alpha = \frac{Q}{2k}\frac{\partial^2}{\partial z^2}\frac{\varepsilon}{z} = \frac{Q}{2k}\frac{2\varepsilon}{z^3}$ is proportional to the local dielectric constant of the material. Analyzing Figure 20, we can see that, in the NCD inter-granular regions, α is similar to that of the graphene, again corroborating the presence of sp^2 phases between the diamond grains. However, it is also found that the diamond dielectric constant seems lower than that of graphene, a counterintuitive observation as graphene is an excellent conductor and diamond an insulator known for its high dielectric constant. In fact this is true, but these conduction characteristics of graphene are true for in-plane transport and not for the off-plane configuration of the present measurements. Theoretical works suggest that graphene indeed shows a high off-plane dielectric constant, dependent on the number of layers and on the applied electric potential [83].

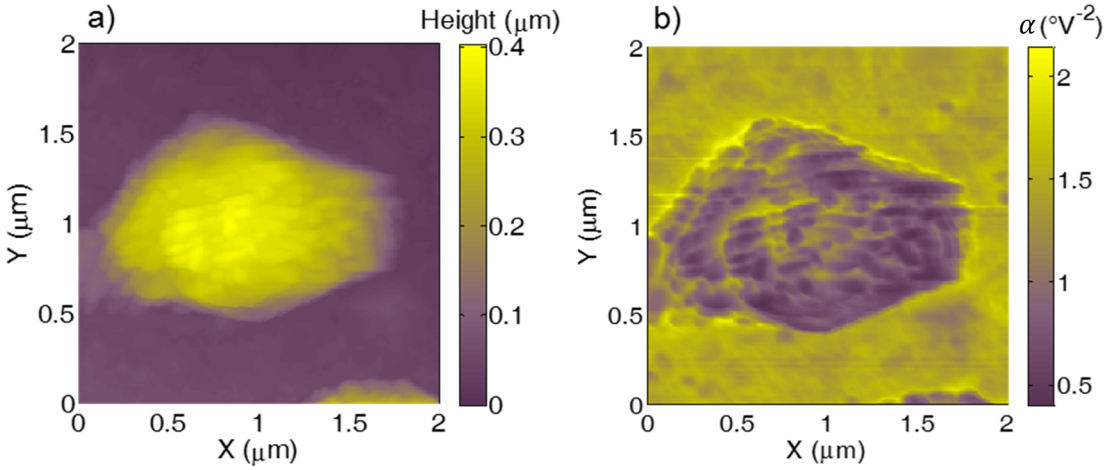

Figure 20. AFM/EFM micrographs of a NCD cluster over graphene. Left, a AFM topographic map; Right, a EFM map of the α parameter ($\frac{Q}{2k}\frac{\partial^2 C}{\partial z^2}$), proportional to the local dielectric constant.

NCD nucleation density control

As described in the Experimental section, four routes have been followed in order to vary the nucleation of the diamond clusters. Following are described the findings for each route.

Increasing the growth time

The main goal of this strategy was to find if it was possible to totally cover the graphene with diamond. While a usual synthesis run lasts for 1 minute, the first try with this approach was carried out for 60 minutes. In fact, it was observed, as expected, an increase of both the NCD clusters density and individual size. SEM images (Figure 21) reveal clusters with diameter

between 5 and 6 µm. This clusters showed to be more hemispherical and uniformly distributed along the surface than in the short growths. In this sample diamond covered 13.5 % of the surface.

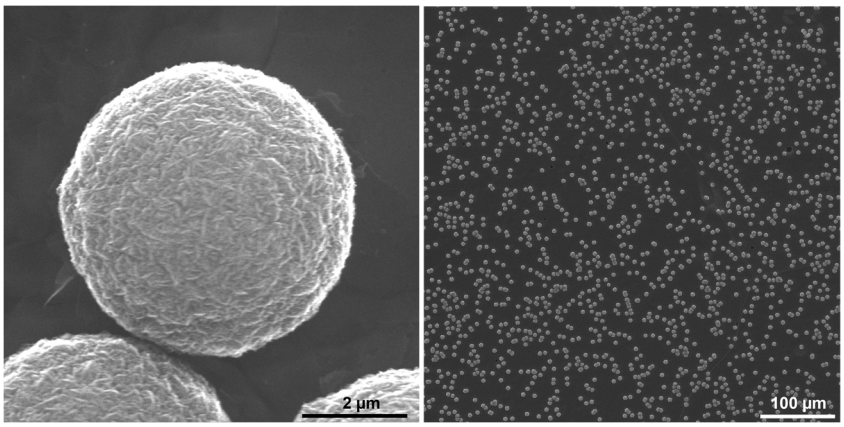

Figure 21. SEM micrographs of GHDs produced by the long synthesis approach (I_2). Left, a detail of a NCD cluster, exhibiting its polycrystalline nature. Right, a low magnification image, showing the distribution of the clusters in the sample, covering 13.5 % of the sample.

During its manipulation, the sample was accidently scratched by the tweezers. This accident allowed further information about the clusters to be extracted. In the left image of Figure 22, we can observe, in profile, a cluster removed by scratching. Here we see the hemispherical nature of the clusters, like in the TEM micrographs, confirming that graphene does in fact connect to the clusters at their base, as a layer can be observed hanging from it. Besides the mechanically removed clusters, some have been removed by thermal stresses during the cool-down step. In the right image of Figure 22 we observe one of such regions where dark spots, possibly multilayered nucleation regions, are present beneath the region before covered by the cluster. This information is in line with the epitaxiality observed in TEM images suggesting that the clusters are formed in the multilayer graphene regions.

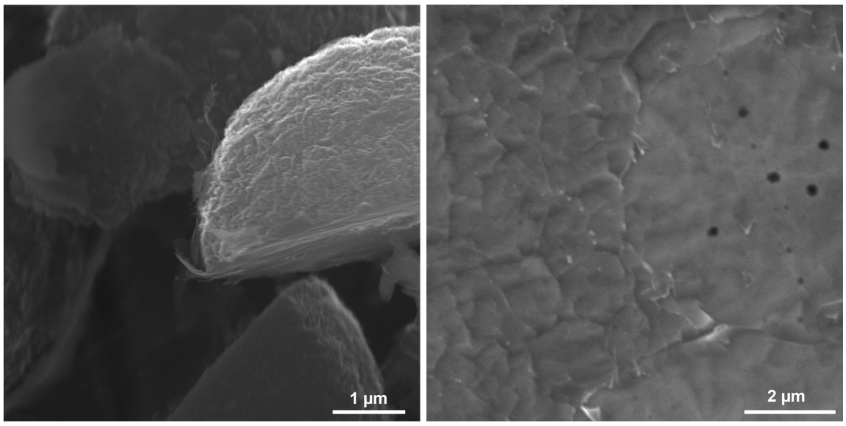

Figure 22. SEM micrographs of a scratched GDH sample (I_2). Left, a profile of a cluster, exhibiting the hemispherical nature. Graphene can be seen suspended underneath the cluster's base. Right, a scar from a region where a cluster was removed by thermal stress. Dark spots suggest that graphene ML nucleation regions are also the nucleation agents of NCD.

The Raman spectra of this sample revealed rather narrow bands for the graphene region (FWHM of 33 cm^{-1}, 17 cm^{-1} and 34 cm^{-1} for the D, G and 2D bands respectively) with no second order splitting as it would be expected for Bernal multilayers, and a I_{2D}/I_G close to 1, as typical of a bilayer. These results are paradigmatic as the sample reveals to be pitch black at naked eye and is fairly opaque in optical microscopy images, as seen in Figure 23. In the same figure, the regions where clusters popped out by thermal stresses appear as clear zones. However they do in fact show the Raman signature of multilayer graphene, further endorsing the connection at the base between the clusters and the graphene. NCD clusters' spectra is now clean from the surrounding graphene signature as they are now larger than the laser spot.

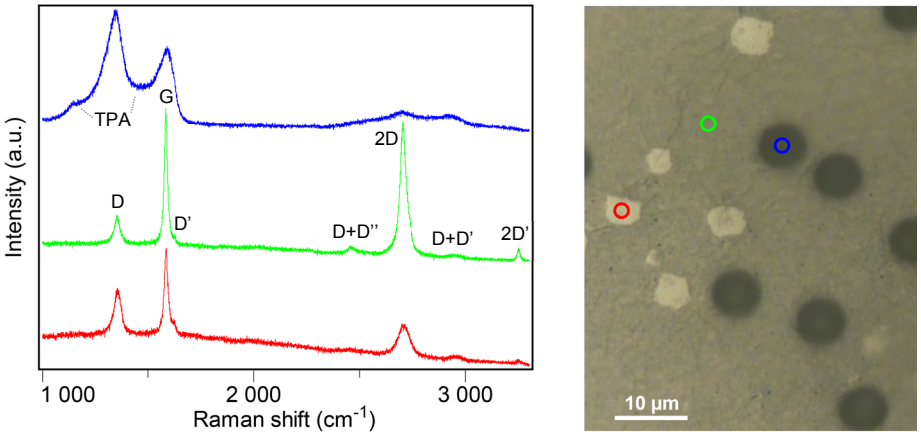

Figure 23. Raman spectra (532 nm) a long deposition approach sample (I_2). Left, spectra of the NCD cluster (blue), graphene regions (green) and removed NCD scar (red). Left, optical image of the scanned regions. Colored circles indicate from where each spectra was acquired.

After this analysis, another run was carried with a growth time of 2 hours. Raman results were similar to the 1 hour run and the sample looked even darker, suggesting more layers.

SEM images revealed that the clusters size did not vary despite the extra hour (Figure 24). Though, a change in the morphology of the clusters was observed: a rosaceous morphology arose from the diamond nano-walls emerging from the cluster, now with a more pronounced topography. Despite this lack of variation in size, the density of the clusters increased as a coverage of 23.4 % was now found, roughly the double of that found on the samples grown for one hour synthesis. Additionally, it is observed that the clusters are starting to merge, forming larger agglomerates. This suggests that longer times will lead to a total coalescence of the clusters, thus closing the diamond film over the graphene as desired. However, at this rate it, would be necessary at least 8 hours of synthesis. Since the operation at powers lower than 1500 W is not advised for long periods in our MPCVD system, this investigation was not performed. In the future, the problem can be solved by installing a microwave directional coupler, allowing the magnetron to operate at high power with only a fraction of it being used by the system.

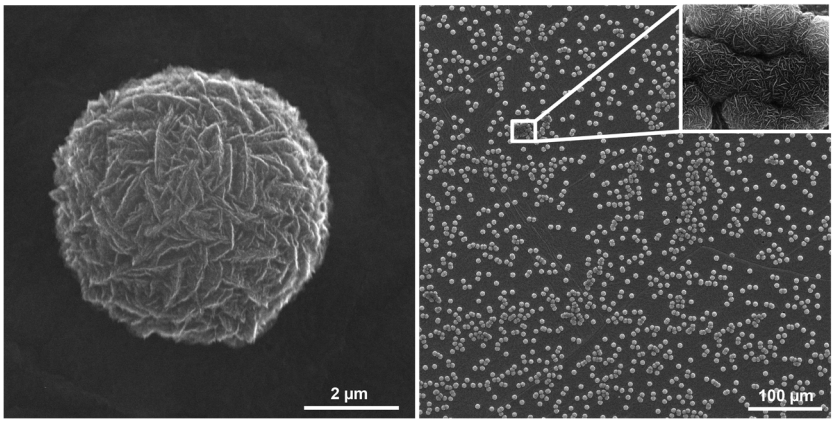

Figure 24. SEM micrographs of a sample with a 2 hour growth time (I_3). Right, a detail of a cluster reveals a higher definition of the crystallites when compared to a 1 hour growth, while almost no variation on the size of the cluster is found. Left, an overall image of the sample reveals a higher nucleation density. Clusters start to merge, as shown in the inset.

Gas mixture change

Gas mixture had almost no impact in the diamond phase, as it was observed after many attempts. It has though revealed to be important in the graphene phase, as increasing the hydrogen started to hinder the graphene formation. This approach was abandoned due to these observations.

Diamond seeding

Ironically, this process, from all the different routes to promote diamond growth, revealed to be the only one resulting in samples with no diamond at all. This reveals that the standard mechanism involved in the nucleation and growth of CVD diamond is different from that in this GDH synthesis. Raman spectra (Figure 25) with a very strong D and D' band were found, suggesting that the graphene film was incomplete. Very small clusters were also found but with a graphite signature instead of that of diamond (Figure 25, right).

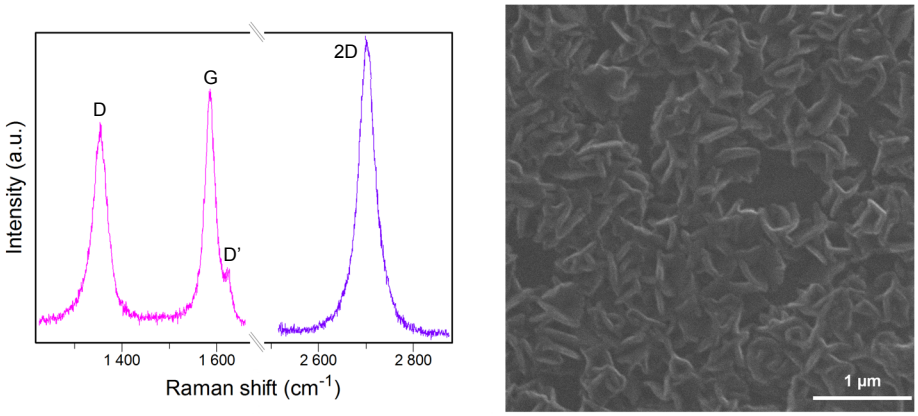

Figure 25. Raman spectra (532 nm) and SEM micrograph of a diamond seeded sample (M_{36}). Left, Raman spectra exhibiting very intense D and D' bands and wide D and 2D bands. Right, SEM micrograph revealing vertical graphene/graphite platelets, compatible with the found D band, as the high amount of exposed edges will increase it.

Growth times were successively increased in an attempt to coalesce the film. Though, the obtained result was a surprise: small clusters of graphene/graphite nanowalls started to form and grow in size for larger times all over the sample (Figure 25). This morphology is compatible with the Raman spectra, as cross planes will expose many edges under the laser spot. This is known to enhance the D and D' bands, as reported in literature for vertically aligned graphene [84]. With this results, the seeding protocol was found to be inadequate for the goal of the present project.

Phased growth

This process, as expected, was successful in increasing the diamond phase expression, with a 13.3 % coverage being observed (Figure 26). Various recipes were followed leading to similar structures. However, reproducibility was not found: the variations within a given recipe covered the observations done in the others. This lack of reproducibility has two main probable causes. First, as the stages have durations in the same order of the gas flow controller response time, each run outcome will be affected by the response time variability. Besides, by using the graphite ring under the Mo holder, plasma arcs are produced between both, eroding the graphite and thus releasing carbon to the reaction atmosphere. This process is random and completely out of control, and revealed to have an increased impact on the variability of results in the phased growth process. Nonetheless, this process showed to have potential for further exploration if these issues are solved.

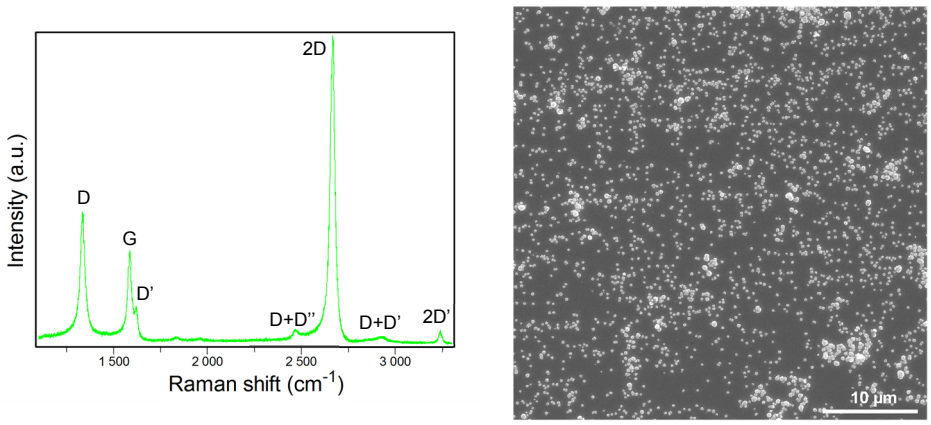

Figure 26. Raman spectra (532 nm) and SEM micrograph of a phased growth sample (M_{50}). Left, Raman spectra exhibiting very intense D and D' bands, but sharp bands and a high I_{2D}/I_G ratio. Right, SEM micrograph revealing a high density of diamond, despite the much shorter time, when compared to the 1 or 2 hours regular growth.

Raman spectra show an increased D and D' band on most samples (Figure 26). This observation is easily explained, as during the H_2-only phase the graphene etching is promoted, thus, boosting the number of defects. The unusually high $I_D/I_{D'}$ ratio suggests that the new defects are indeed structural, not corresponding to hydrogen adatoms [72]. The high defect density is the main disadvantage of this strategy, as all samples displayed a high defect density according to Raman.

GFET microfabrication and characterization

As already described, the substrate production for the GFETs encountered some practical issues. Figure 27 exhibits various steps of the microfabrication, from the bulk silicon wafer, passing thought the TiWN deposition, DWL exposition, revelation, ion milling, inspection, Al_2O_3 sputtering, gate contact trench inspection, gold sputtering and ion milling, SEM inspection of the alignment problems in the various Al_2O_3 deposition/etching processes, the final wafer, the die separation after dicing and the final substrate.

However, besides the process problems that were found, after the end of the microfabrication, a design issue was detected. The alumina thickness of 30 nm was chosen in order to apply a high field to the graphene with a relatively low voltage, a desirable characteristic for low-power electronics such as sensors. Although, we have to bear in mind that sometimes graphene is doped either during production or transfer processes, causing a V_{Dirac} shift to higher or lower potentials. Thus it is then required for the transistor to be operated centered at high values of $|V_{GS}|$. These two informations collide in a property of the dielectric layer: the dielectric strength, the maximum field a material can withstand without the occurrence of a catastrophic electrical breakdown. The best values found in literature for alumina are in the order of the few hundreds of MV m^{-1}, which means that the expected breakdown voltage for our 30 nm device should be around 6 V [85]. Actually, GFET devices produced from the same wafer failed before reaching V_{Dirac}. However, this was observed using graphene from a different source, probably strongly doped by the transfer process involving $FeCl_3$.

Despite these indications, the process continued by transferring the graphene and GDH sheets to finish the device (Figure 28). Oxygen plasma etching was used for patterning as described in the Experimental section. Despite the standard recipe for etching single layer graphene was used, the processed samples revealed to endure it. Either the samples hydrogenation protected them from the process, or the multilayer nature of the graphene or other reason protected them from the etching process, causing that the patterning had to be mechanically performed by the manual micro-positioner tips.

Luckily, the graphene and GDH hybrids devices showed to respond as almost intrinsic graphene, with a V_{Dirac} very close to 0 V $V_{GS.}$ All the devices worked, although under a set of parameters. For V_{GS} values between -5 and 5 V the devices worked without problems[f], while for higher voltages they failed irreversibly, probably due to the formation of a conduction path after breakdown.

[f] Depending on the device, this value could be higher. ± 5 V was the value found to be safe for all the measured devices.

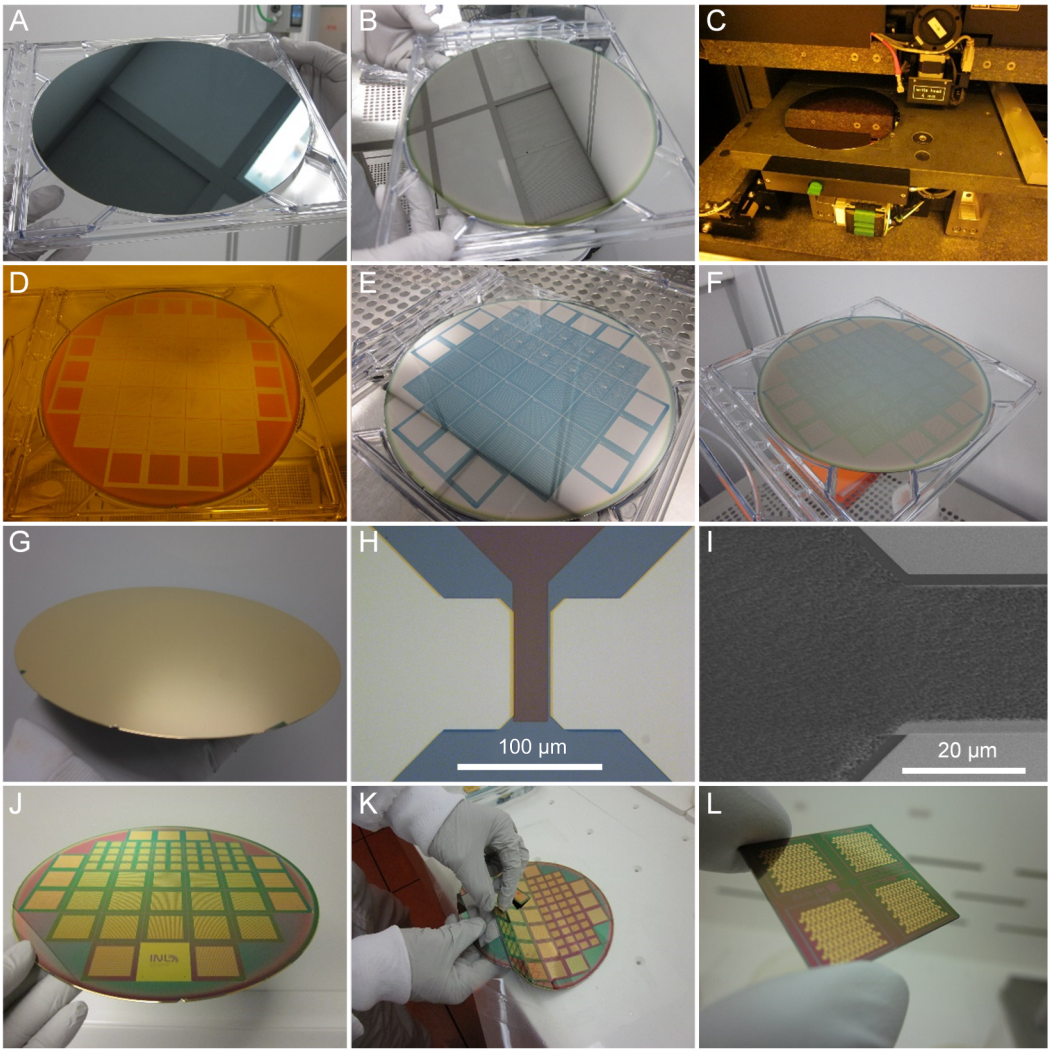

Figure 27. Microfabrication process. A – Starting SiO_2 (200 nm)/Si 200 mm wafer. B – Wafer after TiWN deposition. C – DWL exposure. D – Wafer after exposure and revelation. E – Wafer after the 1st physical etching process. F – Alumina deposited over the wafer. G – Gold deposition. H –Microscope image of the gate after the gold etching. Alumina was also removed. I – SEM micrograph of the gate after the second alumina wet etch process. Below, a misalignment is observed between the photoresist and the gate. This caused alumina etching at the gate. J – Final wafer. K – Die separation after dicing. L – Final die with the 2×2 matrixes of 66 transistors.

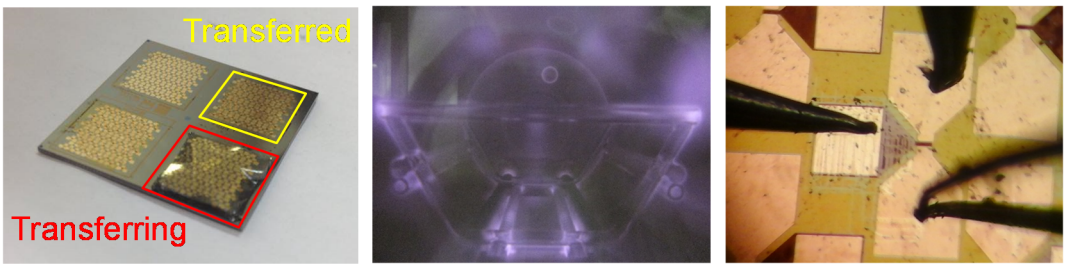

Figure 28. Active layer transfer and patterning. From left to right: GDH film transferred and during the transfer process to the GFET contact substrate; O_2 plasma graphene patterning; Device during transfer curve measurement. Note the mechanically etched gate region.

Figure 29 shows representative output curves of the different studied samples. They have all been shifted in current by removing their $I_{0,}$ as it will be later shown, this value is dependent on the graphene patterning. Rather symmetrical curves were found with the typical V-shape. The left plot in Figure 29 shows different graphene[g] samples curves, while the right one corresponds to samples produced using both phased growth and long times for enhanced NCD nucleation. Mobilities were calculated by measuring the transconductance from the first linear regions for V_{GS} below and above V_{Dirac} and using Equation 1. The mobility value calculated with the g_m extracted from the region of $V_{GS} < V_{\text{Dirac}}$ (negative slope) corresponds to the holes's mobility (μ_h), while the value obtained from $V_{GS} > V_{\text{Dirac}}$ (positive slope) corresponds to the electron's mobility (μ_e). In all cases, the obtained values for both electron and hole mobilities were somehow disappointing, as they are lower than that of silicon for all samples [86]. A correlation was found between the graphene quality, hinted by Raman spectroscopy, and the measured carrier mobilities. Small to null V_{Dirac} where found in all samples, being the larger shifts observed in samples where graphene O_2 plasma patterning was attempted before the mechanical process, suggesting graphene doping. The overall low mobility of the samples probably arises by the same reasons as the D band: either hydrogenation or structural defects, both promoters of conduction bottlenecks. Highly nucleated NCD samples revealed an overall tendency for lower mobilities. This is a natural result as the covalent binding of diamond to graphene will hinder the carriers' mobility just like hydrogen terminated dangling bonds.

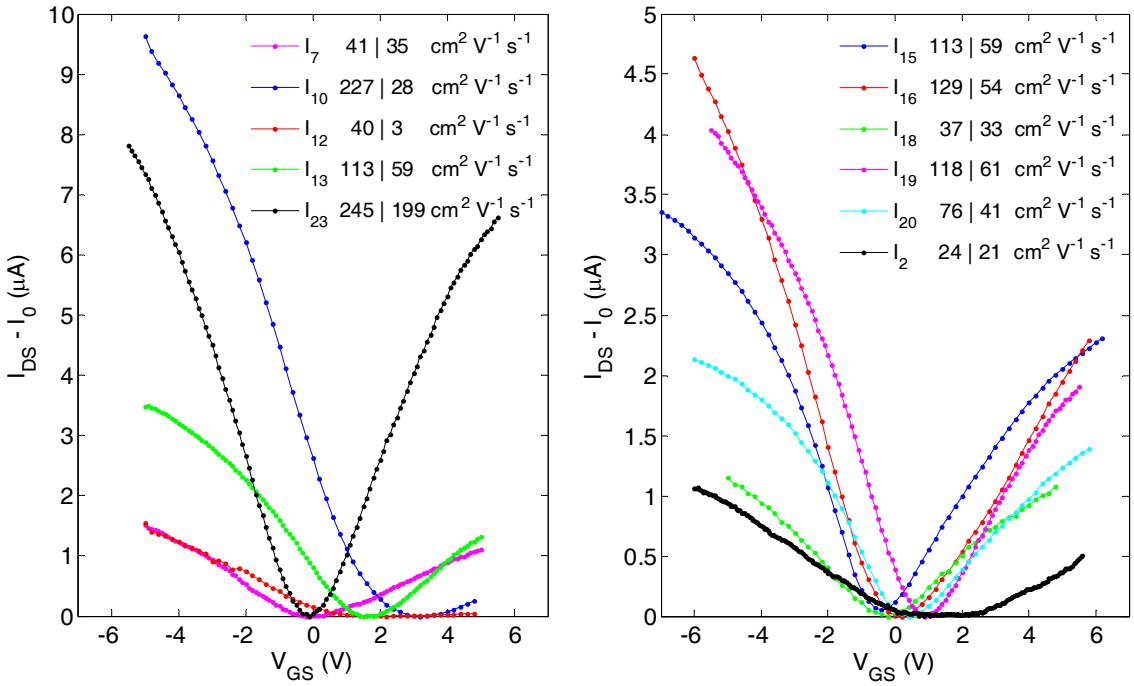

Figure 29. Transfer curves of graphene and GDH samples. Left, graphene samples. Right, GDH samples. Most samples exhibited a symmetric curve with V_{Dirac} close to 0 V, suggesting low doping. Sample reference is indicated on the legend of each graphic.

[g] Samples with a very low NCD content will be called graphene samples.

Care shall also be taken when looking to the calculated mobilities, as it was assumed a parallel plate model for the calculation of the capacitance, which might be in fact different from the real value.

A large variation in values for the minimum I_{DS} in each curve was found in transistors from the same sample. This disparity was found to be related with the mechanical patterning (Figure 30). The extension of graphene removal influences the transistor current offset. This effect comes from the surrounding ungated graphene that behaves as a constant resistor in parallel to the GFET, increasing the overall current value by a constant: the more ungated graphene between the source and drain, the lower the resistance and consequently the higher the current.

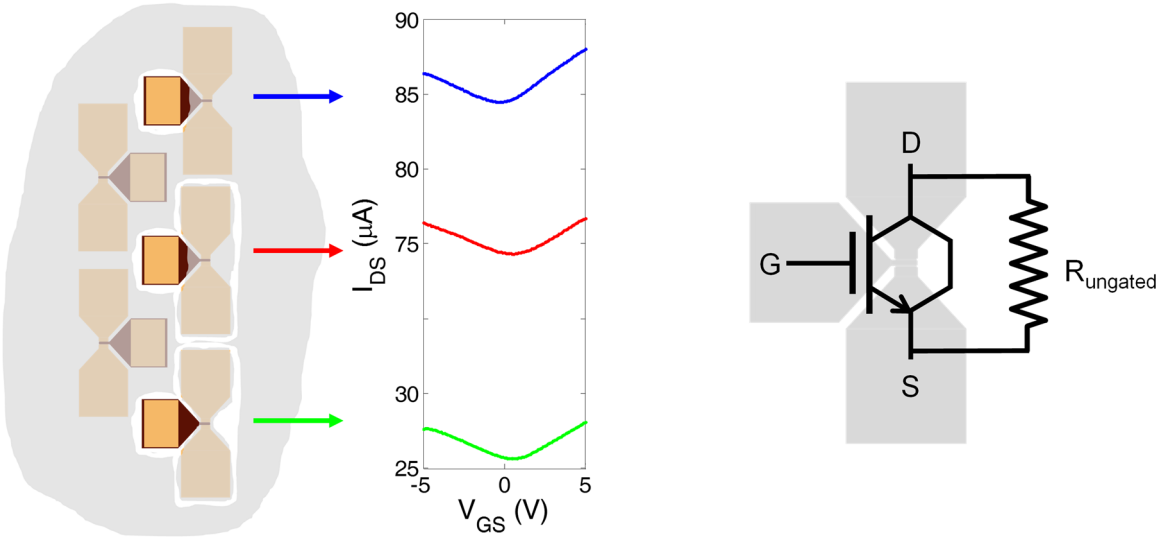

Figure 30. Graphene patterning effect on the minimum current. Left, three stages of patterning and corresponding transfer curve (all done in the same transistor). Further material removal from around the gate reduces the overall current. The curve shape is although kept. Right, model of the actual device, where $R_{ungated}$ is the parallel resistance added by the not removed ungated graphene.

One of the effects that theoretical works predicted from the combination of graphene with diamond was the opening of the band gap [25]. The operation of a GFET is based on the shifting of the Fermi level to energies with a different density of states. At the graphene's Dirac point this density of states is null, like in the gap of any material. If a gap is induced in the graphene, the low conductance state should be kept for all V_{GS} that keep the Fermi level inside the gap. So, the expected form of the transfer curve, assuming the 0 energy level at the tip of the valence band, should follow a shape as described in Figure 31. In fact, sample I_2 exhibited this behavior in two of the three transistors that could be measured. This sample, belonging to the set of the extended growth approach, showed a flat minimum conduction region from 0 to 2.6 V, although with a very low device mobility.

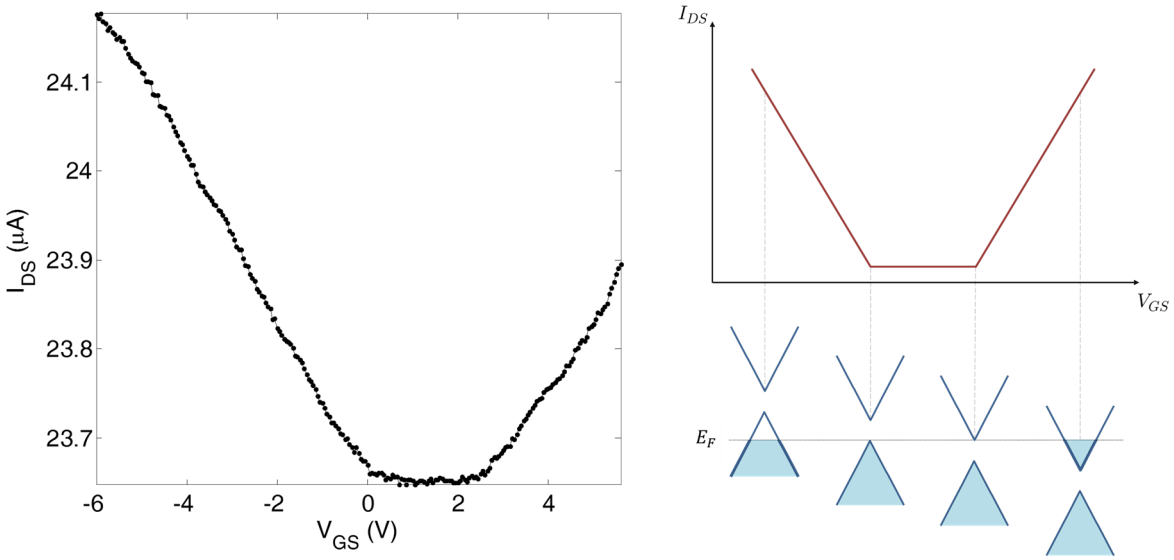

Figure 31. Gap opening in GDH. Left, measured transfer curve for the long time growth sample I_2, exhibiting a flat minimum conduction region. Right, expected transfer curve for graphene with gap: while the Fermi level is in the gap, the conductivity is kept at minimum and constant.

Conclusions and Future Work

The main goal of this work was to study different routes for the simultaneous synthesis of graphene diamond hybrids by MPCVD and to study their structural, morphological and electrical properties with the production of GFETs. SEM, TEM, AFM, EFM, Transmitance and Raman spectroscopy results found the presence of hydrogenated incommensurable graphene multilayers having a strong connection with the polycrystalline NCD clusters. Low carrier mobilities were found by the analysis of the GFET transfer curve, easily explained by the hydrogenation of the sample which induces conduction bottlenecks. Two methods were discovered to be able to control the diamond clusters density, one, based on the phased growth between sp^2 and sp^3 promoting gas mixtures, and other on long synthesis periods. The first method revealed to be a fast way to produce highly NCD nucleated materials, however showing a large output window for a given set of parameters due to experimental issues. The long time synthesis approach has shown to be effective in the growth of the diamond phase and transfer curves exhibited a behavior compatible with the presence of a band gap.

Further studies are required in this material, having both synthesis strategies shown promising results, only hindered by specific and solvable equipment limitations.

As future work it is suggested to:

- Study the field emitting properties of the hybrid, taking advantage of both its intrinsic properties and morphology;
- Search for conditions suitable for the diamond film to cover all the area of the sample, producing in this way a graphene-on-dielectric film in one step;
- Increase the samples size, in search for both uniformity and control over the synthesis;
- Verify the observed gap induction by increasing the statistics of the observed data;
- Quantify the hydrogenation of graphene and relate it with the electric properties and Raman signal;
- Investigate the thermal and mechanical properties of the hybrid;

Appendix A – Synthesis Parameters

As the extensive report of the synthesis parameters for all the 114 samples synthesized in the scope of this work would be uninformative by the sheer amount of information, it was decided to only summarize the samples whose results are directly reported in this written report.

Table A.1 Synthesis parameters of some graphene and GDH samples in the ASTeX AX 6350 reactor.

Sample	MW Power (W)	Total pressure (Torr)	H_2 flow (sccm)	CH_4 flow (sccm)	Annealing time (s)	Reaction time (s)		Comment/ Sample set
						$CH_4 + H_2$	H_2	
$\mathbf{I_2}$	1100	28.3	200	20	180	3600	–	Long time
$\mathbf{I_3}$	1100	28.4	200	20	180	7200	–	Long time
$\mathbf{I_7}$	1100	28.0	200	25	240	30	–	Low NCD
$\mathbf{I_{10}}$	1100	27.5	200	25	240	30	–	Low NCD
$\mathbf{I_{11}}$	1100	28.0	200	25	240	40	–	Low NCD
$\mathbf{I_{13}}$	1100	28.0	200	25	240	40	–	Low NCD
$\mathbf{I_{15}}$	1100	27.5	200	25	180	150 30	60 15	Phased
$\mathbf{I_{16}}$	1100	27.5	200	25	180	150 60 45	60 30	Phased
$\mathbf{I_{18}}$	1100	27.5	200	25	180	150 30	60 15	Phased
$\mathbf{I_{20}}$	1100	28.5	200	36	300	20 20 20 20 20 20 20 30	20 20 20 20 20 20 20	Phased
$\mathbf{I_{23}}$	1100	27.5	200	25	180	90	–	2×2 cm^2 Low NCD
$\mathbf{M_{50}}$	1100	28.0	195	25	180	150	60	Phased
$\mathbf{M_{36}}$	1100	28.5	195	25	180	600	–	Seeded

References

[1] H. W. Kroto, J. R. Heath, S. C. O'Brien, R. F. Curl, and R. E. Smalley, "C 60: buckminsterfullerene", *Nature*, vol. 318, pp. 162–163, 1985.

[2] L. Radushkevich, "O strukture ugleroda, obrazujucegosja pri termiceskom razlozenii okisi ugleroda na zeleznom kontakte", *Zurn Fis. Chim*, vol. 26, pp. 88–95, 1952.

[3] P. Wallace, "The band theory of graphite", *Phys. Rev.*, vol. 71, no. 9, pp. 622–634, 1947.

[4] K. S. Novoselov, A. K. Geim, S. V Morozov, D. Jiang, Y. Zhang, *et al.*, "Electric field effect in atomically thin carbon films", *Science*, vol. 306, no. 5696, pp. 666–669, 2004.

[5] Class for Physics of the Royal Swedish Academy of Sciences, "Graphene - Scientific Background on the Nobel Prize in Physics 2010", *R. Swedish Acad. Sci.*, no. October, 2010.

[6] X. Du, I. Skachko, A. Barker, and E. Y. Andrei, "Approaching ballistic transport in suspended graphene", *Nature nanotechnology*, vol. 3, no. 8. pp. 491–495, Aug-2008.

[7] K. Novoselov, "Graphene: The Magic of Flat Carbon", *Interface-Electrochemical Soc.*, vol. 14, pp. 45–46, 2011.

[8] C. Lee, X. Wei, J. W. Kysar, and J. Hone, "Measurement of the elastic properties and intrinsic strength of monolayer graphene", *Science*, vol. 321, no. 5887, pp. 385–8, 2008.

[9] R. R. Nair, P. Blake, A. N. Grigorenko, K. S. Novoselov, T. J. Booth, *et al.*, "Fine structure constant defines visual transparency of graphene", *Science*, vol. 320, no. 5881, p. 1308, 2008.

[10] A. K. Geim and K. S. Novoselov, "The rise of graphene", *Nat. Mater.*, vol. 6, no. 3, pp. 183–191, 2007.

[11] L. A. Ponomarenko, F. Schedin, M. I. Katsnelson, R. Yang, E. W. Hil, *et al.*, "Chaotic Dirac Billiard in Graphene Quantum Dots", *Science*, vol. 320, p. 358, 2008.

[12] M. F. El-Kady, V. Strong, S. Dubin, and R. B. Kaner, "Laser scribing of high-performance and flexible graphene-based electrochemical capacitors", *Science*, vol. 335, no. 6074, pp. 1326–30, 2012.

[13] D. Varshney, C. Venkateswara Rao, M. J.-F. Guinel, Y. Ishikawa, B. R. Weiner, *et al.*, "Free standing graphene-diamond hybrid films and their electron emission properties", *J. Appl. Phys.*, vol. 110, no. 4, p. 044324, 2011.

[14] K. V Emtsev, A. Bostwick, K. Horn, J. Jobst, G. L. Kellogg, *et al.*, "Towards wafer-size graphene layers by atmospheric pressure graphitization of silicon carbide", *Nat. Mater.*, vol. 8, no. 3, pp. 203–207, 2009.

[15] Y. Zhang, L. Zhang, and C. Zhou, "Review of chemical vapor deposition of graphene and related applications", *Acc. Chem. Res.*, vol. 46, no. 10, pp. 2329–2339, 2013.

[16] R. Muñoz and C. Gómez-Aleixandre, "Review of CVD synthesis of graphene", *Chem. Vap. Depos.*, vol. 19, no. 10–12, pp. 297–322, 2013.

[17] S. Bae, H. Kim, Y. Lee, X. Xu, J. Park, *et al.*, "Roll-to-roll production of 30-inch graphene films for transparent electrodes", *Nat. Nanotechnol.*, vol. 5, no. 8, pp. 574–8, 2010.

[18] J. N. Coleman, "Liquid exfoliation of defect-free graphene", *Acc. Chem. Res.*, vol. 46, no. 1, pp. 14–22, 2013.

[19] S. Stankovich, D. A. Dikin, R. D. Piner, K. A. Kohlhaas, A. Kleinhammes, *et al.*, "Synthesis of graphene-based nanosheets via chemical reduction of exfoliated graphite oxide", *Carbon*, vol. 45, no. 7, pp. 1558–1565, 2007.

[20] V. Kaushik and A. K. S. V. D. Vankar, "Microwave plasma CVD-grown graphene – CNT hybrids for enhanced electron field emission applications", pp. 2197–2205, 2014.

[21] T. Shiga, S. Konabe, J. Shiomi, T. Yamamoto, S. Maruyama, *et al.*, "Graphene-diamond hybrid structure as spin-polarized conducting wire with thermally efficient heat sinks", *Appl. Phys. Lett.*, vol. 100, no. 23, p. 233101, 2012.

[22] A. J. S. Fernandes, M. Pinto, M. A. Neto, F. J. Oliveira, R. F. Silva, *et al.*, "Nano carbon hybrids from the simultaneous synthesis of CNT/NCD by MPCVD", *Diam. Relat. Mater.*, vol. 18, no. 2–3, pp. 160–163, 2009.

[23] Q. Wang, N. Plylahan, M. V. Shelke, R. R. Devarapalli, M. Li, *et al.*, "Nanodiamond particles/reduced graphene oxide composites as efficient supercapacitor electrodes", *Carbon*, vol. 68, pp. 175–184, 2014.

[24] J. Yu, G. Liu, A. V Sumant, V. Goyal, and A. A. Balandin, "Graphene-on-diamond devices with increased current-carrying capacity: Carbon sp 2-on-sp 3 technology", *Nano Lett.*, vol. 12, no. 3, pp. 1603–1608, 2012.

[25] Y. Ma, Y. Dai, M. Guo, and B. Huang, "Graphene-diamond interface: Gap opening and electronic spin injection", *Phys. Rev. B*, vol. 85, no. 23, p. 235448, 2012.

[26] F. Schwierz, "Graphene transistors", *Nat. Nanotechnol.*, vol. 5, no. 7, pp. 487–496, 2010.

[27] A. H. Castro Neto, F. Guinea, N. M. R. Peres, K. S. Novoselov, and A. K. Geim, "The electronic properties of graphene", *Rev. Mod. Phys.*, vol. 81, no. 1, pp. 109–162, 2009.

[28] N. D. Mermin, "Crystalline Order in Two Dimensions", *Phys. Rev.*, vol. 176, pp. 250–254, 1968.

[29] V. Ariel and A. Natan, "Electron Effective Mass in Graphene", *arXiv:1206.6100v2 [physics.gen-ph]*, no. 5, pp. 1–2, 2012.

[30] R. Kundu, "Tight binding parameters for graphene", *arXiv:0907.4264v1 [cond-mat.mtrl-sci]*, pp 1–8, 2009.

[31] X. Liang, Y. S. Jung, S. Wu, A. Ismach, D. L. Olynick, *et al.*, "Formation of bandgap and subbands in graphene nanomeshes with sub-10 nm ribbon width fabricated via nanoimprint lithography", *Nano Lett.*, vol. 10, no. 7, pp. 2454–2460, 2010.

[32] Y. Wu, Y. Lin, A. A. Bol, K. A. Jenkins, F. Xia, *et al.*, "High-frequency, scaled graphene transistors on diamond-like carbon", *Nature*, vol. 472, no. 7341, pp. 74–78, 2011.

[33] Y. Lin, C. Dimitrakopoulos, K. A. Jenkins, D. B. Farmer, H. Chiu, *et al.*, "100-GHz Transistors from Wafer-Scale Epitaxial Graphene", *Science*, vol. 327, p. 662, 2010.

[34] A. A. Balandin, "Thermal properties of graphene and nanostructured carbon materials", *Nat.Mater.*, vol. 10, no. 8, pp. 569–581, 2011.

[35] M. Liu, V. I. Artyukhov, H. Lee, F. Xu, and B. I. Yakobson, "Carbyne from first principles: Chain of c atoms, a nanorod or a nanorope", *ACS Nano*, vol. 7, no. 11, pp. 10075–10082, 2013.

[36] G.-H. Lee, R. C. Cooper, S. J. An, S. Lee, A. van der Zande, *et al.*, "High strength chemical vapor deposited graphene and grain boundaries", *Science*, vol. 340, no. 6136, pp. 1073–1076, 2013.

[37] M. Regmi, M. F. Chisholm, and G. Eres, "The effect of growth parameters on the intrinsic properties of large-area single layer graphene grown by chemical vapor deposition on Cu", *Carbon*, vol. 50, no. 1, pp. 134–141, 2012.

[38] B. Hu, H. Ago, Y. Ito, K. Kawahara, M. Tsuji, *et al.*, "Epitaxial growth of large-area single-layer graphene over Cu(1 1 1)/sapphire by atmospheric pressure CVD", in *Carbon*, 2012, vol. 50, no. 1, pp. 57–65.

[39] A. Kumar, A. A. Voevodin, D. Zemlyanov, D. N. Zakharov, and T. S. Fisher, "Rapid synthesis of few-layer graphene over Cu foil", *Carbon*, vol. 50, no. 4, pp. 1546–1553, 2012.

[40] J. Kim, M. Ishihara, Y. Koga, K. Tsugawa, M. Hasegawa, *et al.*, "Low-temperature synthesis of large-area graphene-based transparent conductive films using surface wave plasma chemical vapor deposition", *Appl. Phys. Lett.*, vol. 98, no. 9, p. 091502, 2011.

[41] G. D. Yuan, W. J. Zhang, Y. Yang, Y. B. Tang, Y. Q. Li, *et al.*, "Graphene sheets via microwave chemical vapor deposition", *Chem. Phys. Lett.*, vol. 467, no. 4–6, pp. 361–364, 2009.

[42] T. Yamada, J. Kim, M. Ishihara, and M. Hasegawa, "Low-temperature graphene synthesis using microwave plasma CVD", *J. Phys. D. Appl. Phys.*, vol. 46, no. 6, p. 063001, 2013.

[43] D. A. Boyd, W.-H. Lin, C.-C. Hsu, M. L. Teague, C.-C. Chen, *et al.*, "Single-step deposition of high-mobility graphene at reduced temperatures", *Nat. Commun.*, vol. 6, p. 6620, 2015.

[44] D. V. Kosynkin, A. L. Higginbotham, A. Sinitskii, J. R. Lomeda, A. Dimiev, *et al.*, "Longitudinal unzipping of carbon nanotubes to form graphene nanoribbons", *Nature*, vol. 458, no. 7240, pp. 872–876, 2009.

[45] D. Wei, J. I. Mitchell, C. Tansarawiput, W. Nam, M. Qi, *et al.*, "Laser direct synthesis of graphene on quartz", *Carbon*, vol. 53, pp. 374–379, 2013.

[46] X. Li, Y. Zhu, W. Cai, M. Borysiak, B. Han, *et al.*, "Transfer of large-area graphene films for high-performance transparent conductive electrodes", *Nano Lett.*, vol. 9, no. 12, pp. 4359–4363, 2009.

[47] W. R. Jones, D. Jordan, R. H. Jr., and Trevor Jones, "Critical Melting Points and Reference Data for Vacuum Heat Treating", SOLAR ATMOSPHERES INC, 2010.

[48] A. J. S. Fernandes, M. A. Neto, F. A. Almeida, R. F. Silva, and F. M. Costa, "Nano- and micro-crystalline diamond growth by MPCVD in extremely poor hydrogen uniform plasmas", *Diam. Relat. Mater.*, vol. 16, no. 4–7 SPEC. ISS., pp. 757–761, 2007.

[49] Y. Shao, J. Wang, H. Wu, J. Liu, I. A. Aksay, *et al.*, "Graphene Based Electrochemical Sensors and Biosensors: A Review", *Electroanalysis*, vol. 22, no. 10, pp. 1027–1036, 2010.

[50] J. Fan, S. Liu, and J. Yu, "Enhanced photovoltaic performance of dye-sensitized solar cells based on TiO2 nanosheets/graphene composite films", *J. Mater. Chem.*, vol. 22, no. 33, p. 17027, 2012.

[51] K. J. Tielrooij, J. C. W. Song, S. A. Jensen, A. Centeno, A. Pesquera, *et al.*, "Photoexcitation cascade and multiple hot carrier generation in graphene", *Nat. Phys.*, vol. 9, no. 4, pp. 248–252, 2013.

[52] C.-H. Liu, Y.-C. Chang, T. B. Norris, and Z. Zhong, "Graphene photodetectors with ultra-broadband and high responsivity at room temperature", *Nat. Nanotechnol.*, vol. 9, no. 4, pp. 273–278, 2014.

[53] K. S. Kim, Y. Zhao, H. Jang, S. Y. Lee, J. M. Kim, *et al.*, "Large-scale pattern growth of graphene films for stretchable transparent electrodes", *Nature*, vol. 457, no. 7230, pp. 706–710, 2009.

[54] Q. Zhou and A. Zettl, "Electrostatic graphene loudspeaker", *Appl. Phys. Lett.*, vol. 102, no. 22, p. 223109, 2013.

[55] X. Zang, Q. Zhou, J. Chang, Y. Liu, and L. Lin, "Graphene and carbon nanotube (CNT) in MEMS/NEMS applications", *Microelectron. Eng.*, vol. 132, pp. 192–206, 2015.

[56] A. Tzalenchuk, S. Lara-Avila, A. Kalaboukhov, S. Paolillo, M. Syväjärvi, *et al.*, "Towards a quantum resistance standard based on epitaxial graphene", *Nat. Nanotechnol.*, vol. 5, no. 3, pp. 186–189, 2010.

[57] D. Cohen-Tanugi and J. C. Grossman, "Water desalination across nanoporous graphene", *Nano Lett.*, vol. 12, no. 7, pp. 3602–8, 2012.

[58] G. A. J. Amaratunga, "A dawn for carbon electronics?", *Science*, vol. 297, no. 5587, pp. 1657–1658, 2002.

[59] C. A. Klein and G. F. Cardinale, "Young's modulus and Poisson's ratio of CVD diamond", *Diam. Relat. Mater.*, vol. 2, no. 5–7, pp. 918–923, 1993.

[60] R. P. Mildren and J. R. Rabeau, "Intrinsic Optical Properties of Diamond", in *Optical Engineering of Diamond*, Wiley-VCH GmbH & Co. KGaA., 2013, pp. 2–3.

[61] D. J. Twitchen, C. S. J. Pickles, S. E. Coe, R. S. Sussmann, and C. E. Hall, "Thermal conductivity measurements on CVD diamond", *Diam. Relat. Mater.*, vol. 10, no. 3–7, pp. 731–735, 2001.

[62] D. Selli, I. Baburin, S. Leoni, Z. Zhu, D. Tománek, *et al.*, "Theoretical investigation of the electronic structure and quantum transport in the graphene-C(111) diamond surface system", *J. Phys. Condens. Matter*, vol. 25, no. 43, p. 435302, 2013.

[63] D. Takeuchi, H. Kato, G. S. Ri, T. Yamada, P. R. Vinod, *et al.*, "Direct observation of negative electron affinity in hydrogen-terminated diamond surfaces", *Appl. Phys. Lett.*, vol. 86, no. 15, pp. 1–3, 2005.

[64] D. Berman, S. A. Deshmukh, S. K. R. S. Sankaranarayanan, A. Erdemir, and A. V Sumant, "Macroscale superlubricity enabled by graphene nanoscroll formation", *Science*, pp. 1–7, 2015.

[65] Y. Wang, M. Jaiswal, M. Lin, S. Saha, B. Özyilmaz, *et al.*, "Electronic properties of nanodiamond decorated graphene", *ACS Nano*, 2012.

[66] J. R. Ferraro, K. Nakamoto, and C. W. Brown, *Introductory Raman Spectroscopy*. Elsevier, 2003.

[67] A. C. Ferrari and D. M. Basko, "Raman spectroscopy as a versatile tool for studying the properties of graphene", *Nat. Nanotechnol.*, vol. 8, no. 4, pp. 235–246, 2013.

[68] R. Pfeiffer, H. Kuzmany, P. Knoll, S. Bokova, N. Salk, *et al.*, "Evidence for trans-polyacetylene in nano-crystalline diamond films", *Diam. Relat. Mater.*, vol. 12, no. 3–7, pp. 268–271, 2003.

[69] A. C. Ferrari, J. C. Meyer, V. Scardaci, C. Casiraghi, M. Lazzeri, *et al.*, "Raman spectrum of graphene and graphene layers", *Phys. Rev. Lett.*, vol. 97, no. 18, p. 187401, 2006.

[70] F. Tuinstra, "Raman Spectrum of Graphite", *J. Chem. Phys.*, vol. 53, no. 3, pp. 1126–1130, 1970.

[71] D. C. Elias, R. R. Nair, T. M. G. Mohiuddin, S. V Morozov, P. Blake, *et al.*, "Control of graphene's properties by reversible hydrogenation: evidence for graphane", *Science*, vol. 323, no. 5914, pp. 610–613, 2009.

[72] A. Eckmann, A. Felten, A. Mishchenko, L. Britnell, R. Krupke, *et al.*, "Probing the nature of defects in graphene by Raman spectroscopy", *Nano Lett.*, vol. 12, no. 8, pp. 3925–3930, 2012.

[73] J. K. Lee, S. C. Lee, J. P. Ahn, S. C. Kim, J. I. B. Wilson, *et al.*, "The growth of AA graphite on (111) diamond", *J. Chem. Phys.*, vol. 129, no. 23, p. 234709, 2008.

[74] M. Hulman, "Raman spectroscopy of graphene", in *Graphene - Properties, Preparation, Characterisation and Devices*, 2014, pp. 156–183.

[75] R. Rao, R. Podila, R. Tsuchikawa, J. Katoch, D. Tishler, *et al.*, "Effects of layer stacking on the combination raman modes in graphene", *ACS Nano*, vol. 5, no. 3, pp. 1594–1599, 2011.

[76] P. Blake, E. W. Hill, A. H. Castro Neto, K. S. Novoselov, D. Jiang, *et al.*, "Making graphene visible", *Appl. Phys. Lett.*, vol. 91, no. 6, p. 063124, 2007.

[77] K. W. Urban, "Electron microscopy: The challenges of graphene", *Nat. Mater.*, vol. 10, no. 3, pp. 165–166, 2011.

[78] S. Lilliu, C. Maragliano, M. Hampton, M. Elliott, M. Stefancich, *et al.*, "EFM data mapped into 2D images of tip-sample contact potential difference and capacitance second derivative", *Sci. Rep.*, vol. 3, p. 3352, 2013.

[79] M. J. Behr, E. A. Gaulding, K. A. Mkhoyan, and E. S. Aydil, "Hydrogen etching and cutting of multiwall carbon nanotubes", *J. Vac. Sci. Technol. B Microelectron. Nanom. Struct.*, vol. 28, no. 6, p. 1187, 2010.

[80] H. Liu and D. S. Dandy, *Diamond Chemical Vapor Deposition: Nucleation and Early Growth Stages*. New Jersey, U.S.A.: Noyes Publications, 1995.

[81] Y. Wang, Y. Zheng, X. Xu, E. Dubuisson, Q. Bao, *et al.*, "Electrochemical delamination of CVD-grown graphene film: Toward the recyclable use of copper catalyst", *ACS Nano*, vol. 5, no. 12, pp. 9927–9933, 2011.

[82] S. Rodriguez, S. Vaziri, A. Smith, S. Fregonese, M. Ostling, *et al.*, "A comprehensive graphene FET model for circuit design", *IEEE Trans. Electron Devices*, vol. 61, no. 4, pp. 1199–1206, 2014.

[83] E. J. G. Santos and E. Kaxiras, "Electric-field dependence of the effective dielectric constant in graphene", *Nano Lett.*, vol. 13, no. 3, pp. 898–902, 2013.

[84] P. Hojati-Talemi and G. P. Simon, "Preparation of graphene nanowalls by a simple microwave-based method", *Carbon*, vol. 48, no. 14, pp. 3993–4000, 2010.

[85] C. S. Bhatia, "Alumina films by sputter deposition with Ar/O2: Preparation and characterization", *J. Vac. Sci. Technol. A Vacuum, Surfaces, Film.*, vol. 7, no. 3, pp. 1298–1302, 1989.

[86] C. Kittel, *Introduction to solid state physics*, 8th ed. John Wiley & Sons, 2005.